NASA
TP
1174
c.1

NASA Technical Paper 1174
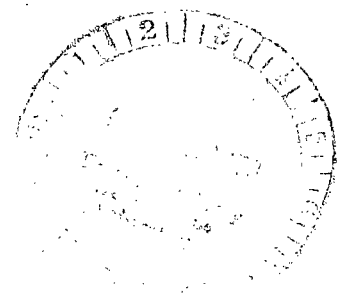
Interaction Between Step Fuel Injectors on Opposite Walls in a Supersonic Combustor Model

Charles R. McClinton

MAY 1978

NASA

NASA Technical Paper 1174

Interaction Between Step Fuel Injectors on Opposite Walls in a Supersonic Combustor Model

Charles R. McClinton
Langley Research Center
Hampton, Virginia

SUMMARY

Results are presented from an experimental investigation of perpendicular,
hydrogen fuel injection and combustion from opposing walls in a scramjet com-
bustor model using a longitudinally staggered laterally inline step-injector
configuration. The model represents a portion of the flow in the Langley inte-
grated modular scramjet engine combustor operating at a flight Mach number of 7.
When operating at a ratio of jet pressure to free-stream dynamic pressure of 3,
the injectors produce a bulk equivalence ratio of unity. This investigation
represents part of a continuing study of the modular engine fuel injectors and
is specifically designed to eliminate the adverse lateral pressure gradient
observed at the injector location in a previous test. Flow survey contours at
three axial locations, ranging from one-third of the engine combustor length to
the total engine combustor length, are used to determine mixing efficiency and
fuel distribution. Wall static pressures are analyzed by using one-dimensional
theory to determine the combustion efficiency. Results show a significant
improvement over previous injector designs tested in this duct geometry.

INTRODUCTION

Scramjet concepts currently being studied at NASA Langley Research Center
are focused on a modular airframe-integrated design (ref. 1). These engines
utilize the vehicle bow shock and flow field for inlet compression, feature
swept surfaces for inlet flow spillage to enhance low-speed inlet starting,
incorporate low internal surface areas to reduce heat load, utilize swept
struts to complete inlet compression and double as fuel injectors, and utilize
the vehicle afterbody as a nozzle extension. Research is continuing on all
phases of the engine design and engine-airframe integration. Fuel injection
and combustion research remains one of the pacing technologies in scramjet
development. Optimum fuel injector design will reduce the scramjet combustor
length and result in significant engine weight saving and reduced engine cool-
ing requirement.

Combustor development remains a semiempirical art. During the past
decade numerous inhouse and contractual studies, both experimental and ana-
lytical, have been performed (for example, refs. 2 to 12). Many of these
studies utilized cold mixing. Because combustion in the scramjet combustor
flow is primarily mixing dependent, initially cold mixing investigations were
used to predict combustor performance. (See refs. 2 to 7.) Some of these
studies used coaxial injectors (ref. 2), some used normal, flat-plate mounted
injectors (refs. 3 to 5), and some used swept struts (ref. 6). Cold mixing
data have also been valuable in developing empirical models for theoretical
analysis of combustor designs. Combustion investigations include basic
research (refs. 8 and 9) and studies applicable to the current scramjet
design (refs. 10 to 12). The investigations in references 8 and 9 set the
groundwork for the parallel and perpendicular modes of fuel injection used
in the modular engine. The latter investigations (refs. 10 to 12) simulated
the swept injectors by using direct-connect combustor testing in the combustion

heater at the Langley Research Center. The investigation presented in reference 10 was performed with injection from an unswept strut. Injector patterns studied incorporated both normal and parallel injection. The investigation presented in reference 11 was performed with injection from a center body which doubled as the facility nozzle and the aft portion of a swept strut. Both of these investigations indicate that the current engine combustor design can produce high combustion efficiencies. The investigation presented in reference 12 studied normal injection with particular attention to the flow geometry and expansion in the first third of the current engine combustor design. The model simulates the flow between two adjacent struts and their downstream slip lines for the modular engine operating at a flight Mach number of 7. As in the modular engine design, on one wall the injector is located upstream of the injector on the other wall. Thus, it is possible to have a strong interaction between the injectors caused by the injection-induced shock and the combustion pressure rise from the upstream injection. On both walls fuel was injected downstream of a step from injector blocks which could be easily modified to allow study of various injector patterns. All fuel injection patterns tested exhibit about 80-percent mixing efficiency over the combustor length tested. But the combustion efficiency exhibited considerable lag, ranging between 41 to 60 percent. Also, all injector configurations tested exhibit inadequate fuel penetration. It was noted in reference 12 that the combined effect of the upstream top-wall injection and the bottom-wall injection was to cancel the lateral static-pressure gradient that exists between the undisturbed air pressure and the low pressure in the recirculation flow directly behind the normal jet. This pressure gradient is believed to play a significant role in initiating the turbulent mixing process.

The current test is a continuation of the normal injector investigation for Mach 7 flight using this step-injector model. The current injector pattern utilizes opposed laterally inline injectors rather than staggered injectors; thus, the downstream injectors are located in a more favorable pressure gradient. Injection from both walls and separate injection from each wall were tested to study the interaction between injectors. Flow surveys were taken at three longitudinal stations, from one-third of the engine combustor length to the total engine combustor length. These survey results are analyzed to produce flow contours of various properties which are then integrated over the flow field to determine the mixing efficiency and combustion efficiency at these combustor stations. Measured wall pressure, temperature, and heat flux are used to deduce the axial distribution of combustion efficiency from a one-dimensional analysis. Experimental results of this investigation are presented and compared with results of reference 12.

SYMBOLS

A   area, m^2

C_f friction coefficient

F   thrust function $(p + \rho V^2)A$, N

H_t total enthalpy, J

h_t, h_b	distance from center line to top and bottom walls, respectively (see fig. 1(b)), cm
M	Mach number
P	combustor wetted perimeter, cm
p	static pressure, MPa
p_t	total pressure, MPa
$p_{t,2}$	stagnation pressure (pitot), MPa
$\dot{Q}$	local heat flux to model, J/m^2-sec
T	static temperature, K
V	velocity, m/sec
w	mass flow rate, kg/sec
x	longitudinal coordinate measured from model entrance (see fig. 1(b)), cm
y	vertical coordinate (see fig. 1(b)), cm
y_0	combustor entrance height, 3.84 cm
z	lateral coordinate (see fig. 1(b)), cm
z_0	combustor width
η_c	combustion efficiency, fraction of injected hydrogen fuel which reacted
η_m	mixing efficiency, fraction of injected hydrogen fuel that would react if complete chemical reaction occurred without additional mixing
ρ	density, kg/m^3
ϕ	equivalence ratio, ratio of fuel mass fraction to fuel mass fraction of a stoichiometric mixture
$X_{H_2,inj}$	local-mass fraction of injected fuel
$X_{H_2,R}$	local-mass fraction of injected fuel which has reacted

Subscripts:

B	bottom fuel injection

corr   pitot-pressure-corrected bow-shock induced reaction

h   combustion heater

j   average or total injector condition

l   model entrance

T   top fuel injection

TG   test gas

w   combustor wall condition

A bar over a symbol refers to mass-averaged values over flow cross section.

APPARATUS AND PROCEDURE

Facility

Hot test gas used in this investigation was provided by a combustion heater fueled by hydrogen, oxygen, and air. Details of the facility, including calibrations, are presented in reference 13. The combustion product contained oxygen in the same volume fraction as is found in air. For this investigation, the facility incorporated a Mach number 2.7 nozzle and is operated at total pressure and temperature of 0.93 MPa and 2117 K, respectively. Nominal test-gas composition was 22.8-percent water vapor, 26.12-percent oxygen, 50.3-percent nitrogen, and 0.88-percent argon by mass with a total mass flow of 2.848 kg/sec. Static pressure and temperature at the nozzle exit were 84.18 kPa and 1082 K, respectively.

Combustor Model

The two-dimensional step-injector combustor model is illustrated and compared with the cross section of the swept Langley modular engine combustor in figure 1(a). The engine side walls and struts are shaded; the combustor model is cross hatched. The model simulates the flow in one passage between the center and side struts. The step injectors are longitudinally staggered as are the strut steps of the engine to simulate injector interactions. A short duct section represents the strut trailing edges. The next downstream combustor section represents the expanding flow between the streamlines from the center and side strut trailing edges. The last two combustor sections are constant-area sections because the facility must exhaust to atmospheric pressure and is already well overexpanded. The engine combustor is 48 strut gaps long; the end of the expanding model section is 20 gaps; and the total model length is 52 gaps. All the combustor model is water cooled except for the injector blocks, constant-area sections, and spacer block on the top wall between the diverging and constant-area sections. Details of the combustor model geometry are presented in table I. The model is 17 cm wide throughout. Top- and bottom-wall coordinates (h_t and h_b, respectively) at each longitudinal

4

location x are presented at each break in the geometry. Also presented are total duct height, cross-sectional area, and wetted perimeter.

Details of the injector block and injector configuration are illustrated in figure 1(b). Both the top- and bottom-wall blocks incorporate a rearward-facing step located 0.381 cm ahead of the 0.295-cm-diameter injection orifices. These steps are incorporated in the engine design to help isolate combustion-induced pressure rise from the inlet. The top-wall step is located 5.08 cm upstream of the bottom-wall step; thus, flow disturbances generated by the top-wall injectors propagating downstream affect the flow seen by the bottom-wall injectors. Four fuel injectors spaced at 4.24 cm, or approximately one simulated strut gap, are located on both injector blocks. Separate hydrogen supply control and metering was incorporated for each injector block. Injector hydrogen flow rates are listed in table II for all conditions tested. For all tests the injected hydrogen was at ambient temperature and 0.896 MPa total pressure. These injectors were sized to produce a bulk stoichiometric flow mixture at a ratio of jet pressure to free-stream dynamic pressure of 3. The same size injectors were used in a test reported in reference 12, listed therein as configuration Q3; however, they were staggered rather than opposed as in this test. Besides similar injector geometry, configuration Q3 results are typical of the best mixing performance obtained in reference 12. They will be used herein for comparisons with the current results.

Instrumentation

Primary flow measurements include (1) instream gas-sample and pitot-pressure surveys, (2) wall static pressure, (3) wall temperature, (4) wall heat transfer, (5) supply gas pressures, temperature and/or flow rates, and (6) cooling water flow rates and temperatures. Most of the data obtained were recorded on digital tape. Because of the large quantity of data, each point could only be read once on the digital tape. Therefore, measurements expected to vary with time throughout the run and a few other key measurements were monitored on strip chart recorders. These measurements included combustor wall temperature, selected combustor wall pressures, and heater and injector total and differential pressures. Pitot pressures were recorded on 14-track FM tape.

Pitot pressure and gas samples were obtained at the exit of the three ducts (see arrows, fig. 1(a)) using the nine-probe rake shown in figure 2. The probe rake is positioned horizontally at the duct exit with the center probe aligned with the combustor vertical center line. Probe tip geometry is illustrated in figure 2. The copper probe tips are cooled by a no-return water flow which dumps in a downstream direction behind the tip shoulder. The tips utilize an internal expansion ratio of 5.76 to quench combustion. Gas samples are also obtained by a nine-orifice static sampling block flush mounted on the end of the top or bottom wall with orifices at the same axial and horizontal position as the pitot probes. Gas samples are collected in two banks of 75-cm^3 pre-evacuated cylinders and analyzed with a gas chromatograph after each run.

Wall static pressure and temperature are generally measured along the center lines of combustor top and bottom walls. In the cooled duct section, some pressure orifices are located off the center line to check flow lateral unifor-

mity. All wall temperatures measured in the cooled duct are located on the inside wall surface along the wall center line. These values rapidly reached equilibrium; thus, they are read and recorded once during the run on the digital tape. Wall temperature measurements in the uncooled duct are made on the outside surface of the duct side wall. These temperatures never reach steady state; therefore, they are recorded on strip chart recorders.

Combustor wall heat flux in the cooled duct is measured at five axial locations on both top and bottom wall by measuring cooling water temperature rise through small flush-mounted wall insert sections. Bulk heat flux to the cooled duct section is determined by heat rise to all the combustor cooling water.

Procedure

Three tests were performed with this combustor geometry. Configuration I used injection from both walls at a nominal bulk equivalence ratio of unity. Detailed flow-field surveys were made at three downstream locations; x = 79, 140, and 201 cm. Configuration II had bottom-wall injection only; configuration III, top wall only. In configurations II and III the injector diameter and total pressure were the same as in configuration I; therefore, the fuel mass flow rate in configuration II was the same as the bottom-wall injection mass flow of configuration I and the fuel mass flow rate in configuration III was the same as the top-wall injection mass flow of configuration I. For configuration II, flow-field surveys were made at two longitudinal stations, x = 79 and 201 cm. For configuration III, no flow surveys were made. Wall pressure, temperature, and heat flux were measured for all three configurations.

The test procedure used follows: (1) establish the burner test-gas flow; (2) start fuel injection and move the probe rake into the flow; (3) delay 1 second to allow the injector flow and combustion to settle and time to measure pitot pressure; and (4) start data acquisition and gas-sample collection. The preevacuated sample bottles are purged to vacuum for 2 seconds and then filled for 6 seconds. Total run time is 14 seconds. The sample bottles are removed for the analysis by the gas chromatograph after the run.

DATA ANALYSIS

Injector performance is assessed by the combustor length required to complete mixing and combustion. Therefore, the longitudinal variation of mixing and combustion efficiency are of primary importance. Two methods of analyzing the data are employed to determine mixing and combustion efficiency and other parameters of interest. One method is a one-dimensional analysis to estimate the distribution of reaction along the combustor length based on measured wall pressure distribution. The other method is numerical integration of the duct-exit flow-field surveys.

One-Dimensional Analysis

A one-dimensional solution to the reacting flow theory was used to determine the average axial flow properties in the combustor. The solution assumes that the fuel and test gas are uniformly mixed at the injection station and uses a stepwise solution of the conservation equations to calculate the reacted equivalence ratio required to match the measured wall pressure, temperature, and heat flux. Other input for this analysis includes fuel and test-gas properties, combustor geometry, and axial wall friction coefficient. The friction coefficient assumed was a constant based on correlations for turbulent flat plate flows, but was adjusted slightly so that the bulk heat flux determined by the modified Reynolds analogy matches the measured heat flux. This analysis neglects pressure losses due to shock waves. A more detailed discussion of the one-dimensional analysis is presented in reference 3.

Exit Flow Integrations

Generally, gas samples are obtained at six rake positions and on the top and bottom wall at each longitudinal survey location. Pitot pressures were obtained at each instream survey point. These survey data are analyzed by assuming uniform static pressure at the survey station, uniform distribution over the flow cross section of the heat lost to the cold walls, and combustion efficiency equal to the one-dimensional analysis result. This analysis produces point values of various flow properties of interest. These flow properties are used to produce flow contours which are integrated to determine total or mass-average values of various properties such as fuel mass flow and mixing efficiency. Details of the data analysis program are discussed in more detail in reference 11.

Acquisition of quenched gas samples, which represent the undisturbed composition existing locally, is difficult, if not impossible, particularly in supersonic reacting flow fields. The probe used is designed to swallow the tip shock wave but it does not. The detached tip shock produced a high indicated degree of reaction and flow spillage (and possibly specie selectivity which occurs even in nonreactive flows), and reduced the indicated stagnation pressure. Three corrections have been incorporated in the data reduction program to account for these effects: (1) The average equivalence ratio over the combustor cross section is set equal to the metered bulk equivalence ratio by uniformly adjusting the local fuel mass fraction at each survey point. (2) The local reacted equivalence ratio is adjusted by using an empirical combustion efficiency model so that the calculated average combustion efficiency is the same as the one-dimensional result. Previous tests have shown that local combustion efficiency is related to the local mixing efficiency and equivalence ratio as illustrated in figure 3. This model illustrates that combustion lags mixing in regions where the equivalence ratio is near stoichiometric. This adjustment affects combustion efficiency; it has no effect on mixing efficiency. It also increases both fuel and test-gas mass flow without changing the equivalence ratio. (3) Pitot pressure is adjusted by assuming the reaction was completed to equilibrium from the undisturbed combustion efficiency determined in item (2). Generally, this adjustment has only a small effect on the mass flows calculated.

7

RESULTS AND DISCUSSION

This section presents experimental results required as input for the one-dimensional analysis and results of the flow-field surveys. Results of the one-dimensional analysis are presented and compared with mass-averaged integrations of the flow-field contours. Comparisons with previous step-injector test results are also presented. Results presented the first compilation of contours at more than one longitudinal location and provide a good test case for computer codes which are capable of predicting three-dimensional turbulent reacting flow fields.

Combustor Wall Pressure

Figure 4 presents combustor top and bottom center-line wall pressures along the entire combustor length for the three injector configurations. On these plots the top-wall data are presented by circles and the bottom-wall data by squares. The distribution used in the one-dimensional analysis, an "educated" fairing of the data, is represented by the solid line. Generally, the wall pressure is characterized by an overall decreasing but scattered pressure in the diverging portion of the duct ($x \leqq 78$ cm). For configurations I and II (figs. 4(a) and 4(b), respectively), the pressure increases rapidly on the bottom wall at the beginning of the constant-area duct ($x = 78$ cm), apparently because of combustion initiated by the 6° shock wave generated at this station. For all configurations the top-wall pressure gradually increases in the constant-area duct section.

Figures 5 and 6 show details of the pressure not readily seen when looking at the entire flow. Figure 5 presents a wave diagram and detailed view of the wall pressure in the diverging duct section along the combustor longitudinal center line. Figure 6 illustrates the lateral pressure distribution in the vicinity of the injectors. In figure 5, the longitudinal wall pressure distributions are presented separately for the top (above wave diagram) and bottom wall (below wave diagram) for the three injector configurations tested, each being compared with corresponding pressure with no injection ($\phi = 0$ solid symbols). A sketch is also presented of a possible shock wave diagram for each injection configuration (except $\phi = 0$). For the no-injection case ($\phi = 0$), the top- and bottom-wall pressures decrease with longitudinal length. Flow adjacent to the top and bottom walls become quite overexpanded for a free jet and appears to separate at about the 55- and 38-cm stations, respectively. These locations represent the first point where the 6° shock generated at $x \approx 25$ cm on the top wall reflects from each wall, which apparently triggers the separation.

Pressure distributions in figure 5(a) for configuration I (both wall injections) illustrate several interesting flow features. Unlike previous tests, the oscillatory nature of the pressure distribution indicates the presence of a system of shock and expansion waves and induced flow separation from the wall. Shock waves accounted for in this sketch are the shocks induced by injection which starts just ahead of the step on the fuel injector blocks – and the shock at the end of the 6° diverging top wall ($x \approx 25$ cm). The shock induced by the top-wall injectors either cancels on the top-wall expansion corner as shown, or combines with the bottom-wall injection-induced shock.

Another interesting feature of these results is the delay between injection and the point where the pressure rises above and remains above the $\phi = 0$ case. In the immediate vicinity of the injector, the pressure rises, apparently from the injection-induced shock interference ($x \approx 5$ cm, bottom wall), but then the wall pressure for configuration I drops back to or below the no-injection case. This is particularly noticeable on the bottom wall, with a length of about 15 cm ($x \approx 25$ cm) before any apparent combustion-induced pressure rise. On the top wall the length is only about 5 cm ($x \approx 8$ cm). Certainly, this delay does not mean there is no combustion for the first 15 cm; more likely, the delay in pressure rise illustrates the three-dimensional nature of the flow at these upstream stations because these center-line wall pressures are measured equidistant between two injectors.

For configuration II (bottom-wall injection only), the wall pressures generally do not exhibit a pressure rise on the top wall above that of the no-injection case, and show only a small rise on the bottom wall (fig. 5(b)). However, the heat addition is sufficient to raise the combustor pressure enough to prevent flow separation due to overexpansion that occurs for the no-injection case. The bottom-wall pressure rise exhibits a similar but smaller delay than observed on the bottom wall for configuration I in figure 5(a).

For configuration III (top-wall injection only), the wall pressures indicate a slight rise on both walls compared with the no-injection case, and a delay in pressure rise on the top wall similar to that observed on the top wall of figure 5(a). (See fig. 5(b).) Again, there does not appear to be any wall flow separation caused by overexpansion. For this configuration, the total fuel mass flow is about 10 percent higher than that for configuration II. This higher fuel mass flow and resulting greater penetration and faster heat release might account for the pressure rise measured on the bottom wall with injection from only the top wall.

Details of the flow field inferred from wall pressures in the vicinity of the injectors are presented in figure 6. Intuitively, the shape of the shock front from the top-wall injectors is as illustrated in figure 5(a), and the shape of the impingement on the bottom wall is as illustrated in figure 5(b). The location of the shock impingement is estimated by using the bottom-wall pressure at the four static-pressure orifices represented in figure 6(b) by "+" symbols. Orifices 1 and 2 are ahead of the shock impingement or flow disturbance for all injection configurations; both indicate pressure equal to the initial pressure p_1. Static pressure measured for orifices labeled "3" and "4," nondimensionalized by p_1, are presented by the bar graph in figure 5(c) for each injector configuration. For no injection, $\phi = 0$, both exhibit pressure about 90 percent of the initial pressure. With top-wall injection only, configuration III, orifice 3 sees higher pressure than orifice 4, indicative of the shock impingement sketch where orifice 3 is downstream of two incident and reflecting shock waves and orifice 4 is located downstream on only one such shock. With bottom-wall injection only, configuration II, orifice 3 measures pressure higher than p_1, but slightly lower than expected for its position behind the shocks induced by the two adjacent jets. Orifice 4 measures pressure less than p_1, a result indicative of its position in the recirculation region induced behind the jet. (See fig. 6(d).) With injection from both walls, configuration I, the pressure at each orifice is between the values mea-

sured for the previous two injector cases. Orifice 4 pressure is a direct result of combining the increased pressure from top-wall injection with the decrease in pressure due to its location in the recirculation region. Orifice 3 pressure is less than the combined pressure rise from top-wall-only and bottom-wall-only injection. However, the magnitude of difference between orifices 3 and 4 is larger for both wall injections than for either the top- or bottom-wall-only configurations. As mentioned in the "Introduction," the goal of this investigation was to obtain faster mixing and combustion by producing a larger lateral pressure gradient at this station than was produced with staggered injectors because in the previous investigation with staggered injectors (ref. 12), the pressure was nearly uniform across the duct at this station with both wall injections. It is clear that the model has the desired lateral pressure gradient.

Injector Block Heating

Heating patterns on the injector blocks are shown in figure 7. Top- and bottom-wall injector blocks are positioned with flow from left to right; thus, when installed, the upper end of the top-wall block is opposite the lower end of the bottom-wall block. The step, fuel injectors, and static-pressure orifices are identified. These heat patterns are the combined result of all the tests performed. Note that both injector blocks are discolored ahead of the step. The top-wall block has negligible surface erosion, but the bottom-wall block has erosion ahead of the step which is indicative of flow separation and combustion. The bottom-wall block also experienced greater heating downstream of the steps, particularly in the high pressure region between the injectors. On the top wall, heating patterns downstream of the injection are prominent only in the corner flow region between the outermost injectors and the wall. This heating pattern for injector T-4 on the top wall does not show clearly in figure 7(a); however, the heating pattern is nearly the same as that for T-1. Injector B-1 on the bottom wall does not exhibit significant wall heating. This is believed to be due to a water leak in the nozzle upstream of this injector. These heating patterns show that combustion starts immediately and spreads rapidly across the duct, at least in the wall boundary layer, particularly on the bottom wall which is influenced by interaction from the top-wall injectors. This interaction apparently separates the boundary layer ahead of the step and allows the injectant and combustion to propagate upstream. This condition produces more rapid initial heat release as evidenced between the bottom-wall injectors.

Combustor Wall Temperature

Nondimensional combustor wall temperatures are presented in figures 8(a) to 8(c) for configurations I, II, and III, respectively. Temperatures measured on the top wall are represented by circle symbols; on the bottom wall, by squares; and no-injection results, by solid symbols. Note that the data presented are for the cooled diverging portion of the duct ($x \leq 78$ cm), except one point (diamond symbols) on the uncooled duct side wall. The solid curve represents the data fairing used as input to the one-dimensional analysis. Wall temperature and heat flux in the uncooled duct sections ($x > 78$ cm) were

determined by matching the transient temperature measurements on the outside
wall of the combustor model by using an iterative numerical solution discussed
in reference 14 to solve the inverse heat-transfer problem, a constant heat
flux being assumed. Within the cooled duct section, the wall temperature is
nearly constant on each wall with axial distance, except for some data scatter.
The bottom-wall temperature without injection exhibits a slight decrease (about
20 K) from the 20-cm to the 75-cm axial station. As expected, the fuel injec-
tion tends to increase the temperature more on the adjacent wall than on the
opposite wall. This is particularly true for configuration II, bottom-wall
injection, figure 8(b), where the top-wall temperature is identical to that for
the no-injection case. Figure 8(c) illustrates that for top-wall injection
only, the top wall experiences an immediate temperature rise and the bottom-
wall temperature is slightly higher than that for the no-injection case at the
20-cm station but continues to increase above the $\phi = 0$ case with axial dis-
tance. For both wall injections (fig. 8(a)), the wall temperature is higher at
all stations on both walls, generally with a larger temperature rise above
$\phi = 0$ at the more downstream stations.

In the uncooled duct section, the thermocouples were located on the side
walls. Thus, they show, more or less, an average of the top- and bottom-wall
temperature. Negligible differences in temperature were measured in this sec-
tion for the various injector configurations or axial locations. For the one-
dimensional analysis, different constant wall temperatures are used for the
cooled and uncooled duct section. A short, arbitrary temperature ramp is
assumed between the two sections.

Wall Heat Transfer

Combustor wall heat flux is presented in figures 9(a) to 9(c) for the
three injector configurations. Experimental data, presented by symbols, are
obtained in the cooled portion of the combustor by measuring heat flux to cool-
ing water flow in small flush-mounted wall insert sections and are obtained in
the uncooled portion by the transient temperature measurements on the wall out-
side surface as discussed in the previous section. The total heat flux in the
cooled, diverging section is determined by total heat flux of the cooling water.
Measured heat flux in the uncooled section is nearly constant with axial loca-
tion so only one value is presented. The solid curve represents results from
the one-dimensional analysis. Values of the wall friction coefficient C_f
used in the one-dimensional analysis to calculate the heat flux by the modified
Reynolds analogy are listed in figure 9. The data exhibit scatter on the order
of 10 to 15 percent from the one-dimensional prediction. Apparently, this data
scatter results from mechanical limitations of the wall inserts used as calo-
rimeters rather than from aerodynamic phenomena associated with the shock
waves. Both single-wall injection configurations exhibit significantly higher
heat transfer on the wall from which the fuel is injected. This result is con-
sistent with the wall temperature and pressure measurements presented in pre-
vious sections. Generally, the measured heat transfer decreased with axial
distance in the cooled duct section. This trend is substantiated by the one-
dimensional analysis and results primarily from the decrease in wall pressure
due to the flow expansion. In the uncooled section, the heat flux calculated
by the one-dimensional analysis is generally less but increases with axial

11

length because of the combustion-induced pressure rise in the constant-area
duct.

Flow Surveys

Flow-field properties at three survey stations are tabulated in the appen-
dix in a format which should be usable for three-dimensional flow modeling com-
puter techniques. As discussed in the data analysis section, these results are
reduced from pitot-pressure and gas-sample data by assuming constant static
pressure, uniform distribution of the heat lost to the cold walls, and entirely
turbulent transport. Flow contours developed from the tabulated data are pre-
sented and analyzed in the remainder of this section.

Flow-field contours of equivalence ratio are presented in figures 10
and 11 for configurations I and II, respectively. No survey data were
obtained for configuration III. For configuration I, contours are presented
at all three duct exits (x = 78.7, 139.7, and 200.7 cm); for configuration II,
at the first and last duct exits. The lateral position of the fuel injectors
is noted by triangular symbols on the top and/or bottom wall. In all cases,
except configuration I at the second duct exit (fig. 10(b)), the flow contours
were generated by using instream pitot and wall static concentration measure-
ments. Figure 10(b) was generated from instream measurements only, treating
the top and bottom wall as reflection or symmetry planes. In all cases, the
side walls are handled as reflection planes. Shaded regions on these contours
represent fuel-rich regions with greater than stoichiometric fuel mass fraction.

Fuel distribution is described in terms of penetration from the combustor
wall and merging between adjacent jets. Ideally, the fuel will initially pen-
etrate into the combustor flow so that each jet has the point of maximum equiv-
alence ratio centered in its assigned rectangular section of the flow cross
section. In this way the fuel can mix in all directions in the cross-section
(yz) plane. Therefore, penetration is described in terms of displacement from
the wall of the point of maximum equivalence ratio. Fuel penetration for con-
figuration I (fig. 10) is about equal from the top and bottom walls, but for
injectors, the fuel penetrated less than one-half the distance between the com-
bustor wall and center line. Adjacent jet mixing regions have merged together
by the first duct exit and the flow rapidly becomes stratified with the highest
equivalence ratio adjacent to the combustor wall. Both factors tend to further
limit fuel mixing to the vertical direction toward the combustor center line.
The maximum value of equivalence ratio is about equal for top- and bottom-wall
injector mixing regions at each survey location and decays from about 1.8 at
the first survey location to 1.5 at the last station.

Fuel penetration for configuration II (fig. 11) is considerably greater
than that for configuration I. Again, the adjacent jet mixing regions merge
and the flow is quite stratified by the first duct exit. As mentioned earlier,
a water leak developed in the bottom left corner of the nozzle during this
investigation. Generally, water leaks displace the fuel; thus, they cause the
low equivalence ratio in the bottom right corner and contributes to the
extremely rapid merging. The maximum equivalence ratio measured at the first
duct exit is about one-half that found for configuration I, and the decay of

the maximum equivalence ratio downstream of this location is slower than that for configuration I.

The equivalence ratio contour for configuration Q3 presented in reference 12 at the first duct exit is repeated herein as figure 12. This figure illustrates distinct mixing regions for each injector. The fuel has penetrated farther across the duct and has not merged with adjacent jets to the extent of the current test. (See fig. 10(a).) Note also, that for configuration Q3 (fig. 12), the top-wall jet exhibits better penetration and faster mixing (lower maximum equivalence ratio) than the bottom-wall injectors. The maximum equivalence ratios for top- and bottom-wall injectors are on the order of 1.5 and 2.5, respectively. For configuration I, both top- and bottom-wall injectors exhibit relatively poor penetration, but the maximum equivalence ratio is only slightly higher than that for the top-wall jets in configuration Q3.

Previous tests in this facility have not used wall static orifice sampling, so it is of interest to compare the results obtained by using wall samples with the previous method of using only instream survey measurements and treating the top and bottom wall as reflection planes. For this purpose, the equivalence ratio contour for configuration I at the first duct exit, produced by the pitot survey data only and treating the top and bottom wall as reflection planes, is presented in figure 13 for comparison with figure 10(a). The reflection method results in higher equivalence ratio at the combustor wall than that measured in the wall static gas samples. This comparison is typical of the other survey results. The effect of this difference on the total flow picture is illustrated by the integrated result comparison in figure 13. The total integrated fuel mass flow rate is about 2.5 percent higher for the reflection method.

Mach number contours are presented in figures 14 and 15 for configurations I and II, respectively. These contours were developed from pitot-pressure measurements by assuming uniform static pressure equal to the wall value at the duct exit. Some subsonic regions exist in the flow, as emphasized by the cross hatching. For configuration I, the subsonic regions first appear as corner flow (fig. 14(a)) and then develop into a full boundary-layer type flow by the last station (fig. 14(c)). The Mach number is higher at both stations for configuration II than for configuration I, but at the third duct exit a large region of subsonic flow nearly covers the bottom half of the flow field. This region appears more like a separated flow than a boundary layer. Generally, these Mach number distributions exhibit no influence from the jets. Rather, they exhibit normal characteristics of a ducted flow, that is, corner flow and pipe type flow. Only the distribution at the upstream station for configuration I (fig. 14(a)) exhibits strong influence of the jets. Configuration II at this station (fig. 15(a)) simply exhibits a vertical Mach number variation with low Mach number near the bottom-wall injectors. These Mach number contours are integrated to determine the mass-averaged Mach number. The mass-averaged Mach number compares favorably with the average Mach number determined by the one-dimensional analysis as illustrated by the comparison listed above each profile.

Several other contour plots were developed, including pitot pressure, fuel mass fraction reacted, fuel mass flow rate, test-gas mass flow rate, density, velocity, and temperature. These contours are numerically integrated over the

entire duct cross section to determine mass-averaged flow parameters for comparisons with results from the one-dimensional analysis. These comparisons are shown in table II. Direct comparisons of combustion efficiency, internal thrust, average total enthalpy, velocity, and pitot pressure illustrate good agreement between the two procedures. A discussion of combustion efficiency and mixing efficiency is presented in a later section.

Strip Integrations

Fuel and test-gas flow rate contours were numerically integrated in horizontal and vertical strips to determine the average vertical and horizontal fuel and test-gas distributions. These distributions provide another means of illustrating injector performance, that is, mixing rate, penetration, and merging. The degree of mixing is represented by the flow distortion of the vertical fuel distribution, measured by the difference between maximum and minimum relative fuel mass flow. Average injectant penetration is illustrated by the distance from the wall to the vertical location of maximum relative fuel mass flow rate. The degree of merging between adjacent jets is defined by the difference between maximum and minimum relative fuel mass flow rates on the lateral fuel distribution.

Vertical relative mass flow rate distributions of fuel and test gas are presented in figure 16 for configurations I and II. Relative mass flow is the ratio of the actual flow within the integrated strip to the flow expected if the fuel and air were mixed uniformly over the entire flow cross section. Vertical fuel and test-gas distributions determined from contours generated by using only instream measurements are presented by the symbols and the solid lines. Distributions from contours which incorporated the wall concentration measurements are presented in figure 16. Although the latter distributions should be more accurate, they are not available for each survey so they should not be used for the following discussion. Fortunately, the two curves are in good agreement on the performance points mentioned above with one exception, the bottom-wall penetration in figure 16(a). In this one exception, results of the wall concentration curve are used.

Vertical distributions of fuel at the three duct exits for configuration I illustrate that the maximum relative mass flow decays from about 1.4 to less than 1.1 whereas the minimum increases from about 0.65 to 0.9 from the first to the third duct. The maximum relative fuel flow shifts slightly toward the combustor center line with axial length. Although configuration I had slightly greater mass flow from the top-wall injectors than from the bottom-wall injectors, at the first duct exit (fig. 13(a)) the surveys indicate that the bottom-wall injectors have more flow than the top-wall injectors. The obvious error is believed to be associated with assuming constant static pressure across the duct exit which has diverging flow on one side only.

Vertical fuel distributions for configuration II are presented in figures 16(d) and 16(e). These distributions show that the fuel penetrates farther and has lower maximum concentration than those for configuration I. Thus, the bottom-wall injector flow has diffused, on this one-dimensional distribu-

tion, to less than stoichiometric (relative mass flow, 1.0). This faster mixing is expected because of the lower average fuel mass fraction.

Lateral fuel distributions for configuration I are presented in figure 17 at the three survey stations by using the same notations as in figure 16. At the first station the location of three of the four jets is apparent by local peaks on the fuel contours and minimums of the test-gas distribution. The rightmost jet is depicted only by a small deflection in the decreasing trend of the fuel distribution and by the local minimum in test-gas distribution. At the two downstream stations, merging is extensive and both the fuel and test-gas lateral distribution take on the shape of normal pipe flow. Similar results were obtained for configuration II, but the faster mixing produced rapid merging, as is obvious from the flow contours of figures 11(a) and 11(b).

Combustion Efficiency

Combustion efficiency obtained by the one-dimensional analysis and by integrations of the flow contours is presented in figure 18 as a function of combustor longitudinal length. Results are presented only for configurations I and II. The integration results, presented by circle symbols, and the one-dimensional results, presented by the solid curve, are in good agreement. For both configurations there is an apparent delay in combustion followed by relatively fast mixing and combustion in the first third of the duct; slower mixing and combustion occur in the last two-thirds of the duct. This trend is in agreement with the trend of η_c asymptotically approaching 1.0. However, it is not consistent with faster combustion expected in the constant-area duct. At the end of the first duct the combustion efficiency is nearly 0.6 for configuration I, but only about 0.45 for configuration II. At this station the mixing efficiency is slightly higher for configuration II (0.84) than for configuration I (0.78). Thus, the configuration with one wall injection produces faster mixing, but slower combustion heat addition. This observation is indicative of faster reaction caused by increased combustor pressure. The increased pressure is caused, in part, by the second jet-induced shock wave system but it primarily results from combustion. In the constant-area duct, the combustion efficiency increases faster than mixing efficiency, particularly for configuration II, so that at the last station η_m and η_c are approximately 0.91 and 0.80, respectively, for both configurations.

Figure 8(a) also presents comparison with configuration Q3 from reference 12. Combustion efficiency and mixing efficiency for configuration Q3 at the end of the first duct section are 0.42 and 0.83, respectively. These values are presented in figure 18 by the solid symbols. The mixing efficiencies for configurations I and Q3 are in reasonable agreement. However, combustion efficiency for configuration I is almost 40 percent greater than that for Q3. This improved combustion apparently results from the larger lateral pressure gradient and induced cross-stream velocity directly downstream of the fuel injector.

15

CONCLUDING REMARKS

Results are presented for an experimental investigation of perpendicular, hydrogen fuel injection and combustion using an axially staggered step-injector configuration. The results are compared with results of previous investigations made in this combustor model by using laterally staggered rather than opposed injectors. The opposed injector configuration eliminated the adverse lateral pressure gradient experienced at the downstream injectors in the staggered injector configuration and strengthened the gradient over that produced by single-wall injection. Detailed flow-field contours are presented for three longitudinal stations located 78.7, 139.7, and 200.7 cm downstream of injection. In previous tests with this combustor, data were obtained only at the 20-gap station. Mixing efficiency at the 20-gap station was not changed from previous results (0.83) but the combustion efficiency changed from 0.42 to 0.58. At the last survey station, which approximates the length of the Langley integrated modular scramjet engine combustor, the mixing efficiency is 0.91, and the combustion efficiency is 0.88. These contours show that the fuel does not penetrate as far into the combustor flow as it did for the staggered injector arrangement, and that the adjacent jets merge more rapidly even though they are at the same lateral spacing. Increasing the lateral spacing should eliminate the vertically stratified fuel distribution at the survey location and increase the mixing rate in the last half of the combustor.

Results presented represent the first compilation of contours at more than one longitudinal location and provide a good test case for computer codes which are capable of predicting three-dimensional turbulent reacting flow fields.

Langley Research Center
National Aeronautics and Space Administration
Hampton, VA 23665
March 8, 1978

APPENDIX

SURVEY DATA

The reduced survey data are presented in tables III, IV, and V for configuration I at the three longitudinal survey stations. These tables are presented to aid in using these data in development of three-dimensional computer codes. Various assumptions used to reduce the raw pitot-pressure and gas-composition measurements are discussed in the text ("Data Analysis" section). The data are presented in a matrix format, with nondimensional coordinates listed. Fuel mass fraction $X_{H_2,inj}$ and measured nondimensional pitot pressure $p_{t,2}/p_{t,h}$

are not corrected. The remainder of the flow properties reflect the corrections to the survey data discussed in the text. Other flow properties presented are: reacted injected hydrogen mass fraction; corrected pitot pressure, the longitudinal component of time-averaged velocity being deduced by assuming uniform static pressure; static temperature being deduced by assuming uniform total temperature; longitudinal component of mass flux; and longitudinal component of local Mach number. The local time-averaged flow direction was not measured, but at these longitudinal stations downstream of injection, it can be assumed to be zero.

REFERENCES

1. Henry, John R.; and Anderson, Griffin Y: Design Considerations for the Airframe-Integrated Scramjet. NASA TM X-2895, 1973.

2. Eggers, James M.; and Torrence, Marvin G.: An Experimental Investigation of the Mixing of Compressible-Air Jets in a Coaxial Configuration. NASA TN D-5315, 1969.

3. Torrence, Marvin G.: Effect of Injectant Molecular Weight on Mixing of a Normal Jet in a Mach 4 Airstream. NASA TN D-6061, 1971.

4. Rogers, R. Clayton: Mixing of Hydrogen Injected From Multiple Injectors Normal to a Supersonic Airstream. NASA TN D-6476, 1971.

5. McClinton, Charles R.: The Effect of Injection Angle on the Interaction Between Sonic Secondary Jets and a Supersonic Free Stream. NASA TN D-6669, 1972.

6. McClinton, Charles R.; Torrence, Marvin G.; Gooderum, Paul B.; and Young, Irene G.: Nonreactive Mixing Study of a Scramjet Swept-Strut Fuel Injector. NASA TN D-8069, 1975.

7. McClinton, Charles R.: Evaluation of Scramjet Combustor Performance Using Cold Nonreactive Mixing Tests. AIAA Paper No. 76-47, Jan. 1976.

8. Beach, H. L., Jr.: Supersonic Mixing and Combustion of a Hydrogen Jet in a Coaxial High-Temperature Test Gas. AIAA Paper No. 72-1179, Nov.-Dec. 1972.

9. Rogers, R. C.; and Eggers, J. M.: Supersonic Combustion of Hydrogen Injected Perpendicular to a Ducted Vitiated Airstream. AIAA Paper No. 73-1322, Nov. 1973.

10. Anderson, Griffin Y.; and Gooderum, Paul B.: Exploratory Tests of Two Strut Fuel Injectors for Supersonic Combustion. NASA TN D-7581, 1974.

11. Anderson, Griffin Y.; Reagon, Patricia G.; Gooderum, Paul B.; and Russin, W. Roger: Experimental Investigation of a Swept-Strut Fuel-Injector Concept for Scramjet Application. NASA TN D-8454, 1977.

12. Anderson, Griffin Y.; Eggers, James M.; Waltrup, Paul J.; and Orth, Richard C.: Investigation of Step Fuel Injectors for an Integrated Modular Scramjet Engine. 13th JANNAF Combustion Meeting, Volume III, CPIA Publ. 281 (Contract N00017-72-C-4401), Appl. Phys. Lab., Johns Hopkins Univ., Dec. 1976, pp. 175-189.

13. Eggers, James M.: Composition Surveys of Test Gas Produced by a Hydrogen-Oxygen-Air Burner. NASA TM X-71964, 1974.

14. Drummond, John Philip: A Method for Improving the Accuracy in Phase Change Heat Transfer Data Through Increased Precision in Thermophysical Property Determinations. M. Eng. in Mech. Eng. Thesis, Old Dominion Univ., 1975.

TABLE I.- STEP-INJECTOR COMBUSTION DUCT GEOMETRY

x, cm	h_t, cm	h_b, cm	$h_t + h_b$, cm	A, m^2	P, cm
0.0	1.93	1.93	3.86	0.00656	41.71
2.54	1.93	1.93	3.86	.00656	41.71
2.54	2.31	1.93	4.24	.00721	42.47
7.24	2.31	1.93	4.24	.00721	42.47
7.62	2.36	1.93	4.29	.00729	42.57
7.62	2.36	2.31	4.67	.00794	43.33
12.32	2.87	2.31	5.18	.00880	44.35
22.86	4.06	3.33	7.39	.01256	48.77
24.13	4.19	3.40	7.59	.01291	49.17
27.94	4.19	3.61	7.80	.01325	49.58
30.10	4.19	3.76	7.95	.01351	49.89
78.74	4.19	7.24	11.43	.01942	56.85
200.66	4.19	7.24	11.43	.01942	56.85

TABLE II.- BULK, AVERAGE, AND ONE-DIMENSIONAL PARAMETERS

[Values in parentheses denote input values]

Parameter	Bulk	Survey integration	1-D analysis
Configuration I, first duct exit			
p_h, MPa	2.137		(2.137)
T_h, K	1082		(1082)
w_h, kg/sec	2.871	2.846	(2.848)
w_j, kg/sec	0.09155	0.09164	
ϕ	0.9721	0.9809	(0.9721)
η_c		0.5774	0.5736
η_m		0.7778	
F/w_h, N-sec/kg	·	2190.6	2161.3
H_t, MJ		8.060	8.011
V, m/sec		1693	1670
$p_{t,2}$, MPa		0.3127	0.2782
Configuration I, second duct exit			
p_h, MPa	2.137		(2.137)
T_h, K	1082		(1082)
w_h, kg/sec	2.838	2.894	(2.848)
w_j, kg/sec	0.09326	0.09255	
ϕ	1.0020	0.9743	(0.9721)
η_c		0.8319	0.742
η_m		0.8460	
F/w_h, N-sec/kg		2144	2096
H_t, MJ		7.907	7.820
V, m/sec		1347	1468
$p_{t,2}$, MPa		0.2882	0.2627
Configuration I, third duct exit			
p_h, MPa	2.137		(2.137)
T_h, K	1082		(1082)
w_h, kg/sec	2.838	2.821	(2.848)
w_j, kg/sec	0.0933	0.0934	
ϕ	1.002	1.008	(0.9721)
η_c		0.7987	0.857
η_m		0.9077	
F/w_h, N-sec/kg		2116.7	2046.6
H_t, MJ		7.969	7.649
V, m/sec		1271	1304
$p_{t,2}$, MPa		0.2675	0.2518

TABLE II.- Concluded

[Values in parentheses denote input values]

Parameter	Bulk	Survey integration	1-D analysis
Configuration II, first duct exit			
p_h, MPa	2.137		(2.137)
T_h, K	1082		(1082)
w_h, kg/sec	2.836	2.679	(2.848)
w_j, kg/sec	0.0435		
ϕ	0.4676	0.4912	(0.4676)
η_c		0.4449	0.472
η_m		0.8438	
F/w_h, N-sec/kg		2101	2111
H_t, MJ		5.792	5.828
V, m/sec		1825	1829
$p_{t,2}$, MPa		0.3404	0.2771
Configuration II, third duct exit			
p_h, MPa	2.137		(2.137)
T_h, K	1082		(1082)
w_h, kg/sec	2.861	2.883	(2.892)
w_j, kg/sec	0.0441	0.0445	
ϕ	0.4698	0.4783	(0.4676)
η_c		0.8187	0.821
η_m		0.9002	
F/w_h, N-sec/kg		1948	2005
H_t, MJ		5.565	5.619
V, m/sec		1377	1579
$p_{t,2}$, MPa		0.3234	0.2561

TABLE III.- REDUCED EXPERIMENTAL DATA, CONFIGURATION I, x = 78.7 cm

(a) Fuel mass fraction

y/y_o	$X_{H_2,inj}$ for z/z_o of -								
	0.052	0.164	0.276	0.388	0.500	0.612	0.724	0.836	0.948
1.00	0.002	0.002	0.022	0.052	0.056	0.041	0.028	0.013	0.002
.889	.026	.053	.031	.071	.057	.062	.021	.046	.013
.667	.036	.043	.017	.033	.015	.035	.011	.034	.026
.500	.010	.023	.006	.022	.005	.020	.002	.017	.012
.389	.015	.033	.022	.023	.021	.020	.022	.021	.024
.222	.040	.071	.034	.057	.041	.063	.039	.056	.028
.111	.070	.079	.069	.053	.061	.064	.064	.058	.036
0	.002	.048	.047	.054	.024	.055	.034	.057	.004

(b) Reacted fuel mass fraction

y/y_o	$X_{H_2,R}$ for z/z_o of -								
	0.052	0.164	0.276	0.388	0.500	0.612	0.724	0.836	0.948
1.00	0.002	0.002	0.017	0.025	0.028	0.017	0.016	0.013	0.002
.889	.017	.026	.015	.030	.028	.031	.016	.021	.013
.667	.014	.019	.015	.013	.014	.014	.011	.013	.017
.500	.010	.017	.006	.017	.005	.016	.002	.015	.012
.389	.014	.013	.017	.017	.016	.016	.017	.016	.017
.222	.017	.030	.013	.028	.018	.031	.016	.028	.016
.111	.031	.030	.031	.026	.031	.031	.031	.029	.014
0	.002	.022	.022	.026	.017	.027	.013	.028	.004

TABLE III.- Continued

(c) Nondimensional measured pitot pressure

y/y_o	$p_{t,2}/p_{t,h}$ for z/z_o of -								
	0.052	0.164	0.276	0.388	0.500	0.612	0.724	0.836	0.948
1.00	*0.053	*0.081	*0.140	*0.081	*0.062	*0.082	*0.127	*0.084	*0.063
.889	.058	.070	.159	.071	.075	.074	.141	.075	.067
.667	.091	.096	.177	.111	.192	.114	.175	.093	.120
.500	.146	.136	.255	.149	.271	.150	.242	.130	.174
.389	.168	.128	.250	.146	.239	.168	.236	.128	.170
.222	.116	.092	.144	.096	.132	.103	.151	.095	.079
.111	.075	.079	.101	.084	.109	.090	.112	.073	.071
0	*.067	*.076	*.090	*.087	*.099	*.094	*.100	*.075	*.069

*Extrapolated from data values.

(d) Nondimensional corrected pitot pressure

y/y_o	$(p_{t,2}/p_{t,h})_{corr}$ for z/z_o of -								
	0.052	0.164	0.276	0.388	0.500	0.612	0.724	0.836	0.948
1.00	0.053	0.081	0.145	0.087	0.066	0.094	0.138	0.084	0.063
.889	.069	.076	.172	.071	.078	.074	.146	.085	.067
.667	.105	.107	.179	.125	.193	.128	.175	.107	.128
.500	.146	.142	.255	.155	.271	.153	.242	.132	.174
.389	.169	.142	.257	.152	.245	.173	.242	.132	.179
.222	.128	.092	.159	.099	.144	.103	.164	.099	.107
.111	.075	.079	.101	.089	.109	.090	.112	.076	.086
0	.067	.085	.099	.092	.106	.099	.114	.078	.069

TABLE III.- Continued

(e) Velocity

y/y_o	V, m/sec, for z/z_o of -								
	0.052	0.164	0.276	0.388	0.500	0.612	0.724	0.836	0.948
1.00	736	1029	1707	1490	1276	1444	1679	1246	864
.889	1154	1388	1829	1393	1437	1425	1708	1417	1072
.667	1471	1567	1819	1575	1843	1600	1698	1464	1626
.500	1574	1696	1808	1758	1805	1734	1661	1610	1722
.389	1754	1671	2102	1748	2068	1820	2067	1635	1865
.222	1663	1634	1739	1643	1770	1720	1828	1637	1492
.111	1454	1506	1715	1522	1765	1606	1800	1418	1317
0	910	1432	1547	1554	1480	1625	1509	1439	976

(f) Static temperature

y/y_o	T, K, for z/z_o of -								
	0.052	0.164	0.276	0.388	0.500	0.612	0.724	0.836	0.948
1.00	2086	2090	2805	2783	2853	2550	2663	2736	2087
.889	2711	2797	2580	2788	2862	2925	2810	2667	2703
.667	2435	2604	2821	2420	2798	2416	2624	2396	2734
.500	2601	2794	2410	2803	2348	2821	2170	2811	2682
.389	2791	2445	2851	2790	2850	2827	2841	2810	2779
.222	2530	2793	2417	2864	2570	2909	2515	2860	2668
.111	2799	2681	2832	2801	2938	2902	2898	2880	2415
0	2087	2692	2683	2811	2772	2839	2411	2871	2253

TABLE III.- Concluded

(g) Mass flux

y/y₀	ρV, kg/m²-sec, for z/z_0 of -								
	0.052	0.164	0.276	0.388	0.500	0.612	0.724	0.836	0.948
1.00	88.7	135.6	169.1	102.4	79.0	117.9	162.0	117.1	107.9
.889	93.8	91.9	192.6	81.2	91.6	85.4	170.0	104.6	97.9
.667	133.4	127.8	201.5	154.4	216.1	156.0	210.4	138.1	153.2
.500	184.7	166.2	300.5	177.4	321.8	177.4	310.1	160.6	206.9
.389	195.5	169.7	259.1	174.7	250.2	193.1	247.7	158.4	196.2
.222	150.5	100.7	184.8	110.7	162.5	110.4	182.8	110.4	133.8
.111	86.0	88.3	108.6	104.1	116.0	100.0	118.0	88.8	115.0
0	115.2	104.0	117.4	106.4	133.0	111.2	144.2	91.1	113.3

(h) Mach number

y/y₀	M for z/z_0 of -								
	0.052	0.164	0.276	0.388	0.500	0.612	0.724	0.836	0.948
1.00	0.831	1.213	1.759	1.279	1.042	1.346	1.703	1.254	0.993
.889	1.079	1.171	1.929	1.102	1.190	1.146	1.764	1.259	1.064
.667	1.441	1.460	1.980	1.602	2.062	1.622	1.948	1.462	1.632
.500	1.760	1.738	2.381	1.827	2.456	1.816	2.308	1.666	1.948
.389	1.916	1.729	2.403	1.807	2.343	1.939	2.331	1.667	1.975
.222	1.627	1.327	1.837	1.397	1.744	1.429	1.876	1.393	1.461
.111	1.158	1.191	1.413	1.304	1.484	1.314	1.509	1.165	1.267
0	1.053	1.262	1.393	1.332	1.455	1.393	1.516	1.188	1.084

TABLE IV.- REDUCED EXPERIMENTAL DATA, CONFIGURATION I, x = 139.7 cm

(a) Fuel mass fraction

y/y_O	$X_{H_2,inj}$ for z/z_O of –								
	0.052	0.164	0.276	0.388	0.500	0.612	0.724	0.836	0.948
0.889	0.037	0.043	0.047	0.048	0.047	0.046	0.038	0.040	0.039
.667	.028	.042	.036	.036	.029	.033	.024	.028	.027
.500	.016	.017	.017	.016	.012	.017	.012	.021	.018
.389	.022	.027	.018	.020	.015	.022	.014	.019	.018
.222	.037	.043	.028	.034	.040	.035	.037	.038	.032
.111	.049	.047	.044	.046	.045	.047	.044	.043	.036

(b) Reacted fuel mass fraction

y/y_O	$X_{H_2,R}$ for z/z_O of –								
	0.052	0.164	0.276	0.388	0.500	0.612	0.724	0.836	0.948
0.889	0.023	0.026	0.028	0.028	0.028	0.027	0.023	0.024	0.024
.667	.018	.025	.022	.022	.018	.020	.018	.018	.018
.500	.015	.015	.015	.014	.012	.015	.012	.017	.015
.389	.017	.018	.015	.017	.014	.017	.014	.016	.016
.222	.023	.026	.018	.021	.024	.022	.023	.023	.020
.111	.029	.028	.026	.027	.027	.027	.026	.026	.022

(c) Nondimensional measured pitot pressure

y/y_O	$p_{t,2}/p_{t,h}$ for z/z_O of –								
	0.052	0.164	0.276	0.388	0.500	0.612	0.724	0.836	0.948
0.889	0.089	0.095	0.103	0.109	0.106	0.110	0.118	0.104	0.086
.667	.094	.114	.137	.151	.155	.156	.174	.134	.108
.500	.123	.134	.174	.190	.203	.181	.183	.123	.111
.389	.121	.133	.201	.184	.210	.156	.199	.128	.098
.222	.093	.109	.123	.134	.120	.112	.109	.099	.087
.111	.088	.092	.100	.112	.106	.103	.098	.092	.090

TABLE IV.- Continued

(d) Nondimensional corrected pitot pressure

y/y_O	$(p_{t,2}/p_{t,h})_{corr}$ for z/z_O of -								
	0.052	0.164	0.276	0.388	0.500	0.612	0.724	0.836	0.948
0.889	0.107	0.106	0.110	0.115	0.113	0.118	0.132	0.117	0.103
.667	.112	.125	.152	.165	.170	.172	.183	.149	.123
.500	.126	.137	.178	.193	.203	.184	.183	.130	.116
.389	.128	.147	.205	.190	.212	.164	.200	.133	.102
.222	.110	.119	.139	.149	.132	.128	.123	.114	.110
.111	.094	.099	.110	.120	.115	.111	.108	.104	.108

(e) Velocity

y/y_O	V, m/sec, for z/z_O of -								
	0.052	0.164	0.276	0.388	0.500	0.612	0.724	0.836	0.948
0.889	1186	1223	1272	1322	1302	1329	1373	1288	1169
.667	1167	1359	1468	1539	1495	1542	1529	1391	1240
.500	1197	1267	1455	1501	1484	1475	1408	1253	1144
.389	1251	1378	1562	1533	1561	1435	1509	1262	1047
.222	1212	1323	1336	1445	1387	1327	1314	1251	1181
.111	1127	1179	1259	1345	1302	1278	1245	1200	1193

(f) Static temperature

y/y_O	T, K, for z/z_O of -								
	0.052	0.164	0.276	0.388	0.500	0.612	0.724	0.836	0.948
0.889	2852	2922	2956	2967	2957	2945	2861	2886	2875
.667	2736	2912	2840	2847	2723	2804	2783	2733	2743
.500	2729	2741	2747	2728	2621	2742	2605	2774	2749
.389	2778	2748	2758	2781	2722	2783	2697	2767	2750
.222	2851	2917	2729	2822	2883	2833	2857	2858	2788
.111	2977	2961	2927	2944	2939	2953	2931	2920	2840

TABLE IV.- Concluded

(g) Mass flux

y/y_0	ρV, kg/m²-sec, for z/z_0 of -								
	0.052	0.164	0.276	0.388	0.500	0.612	0.724	0.836	0.948
0.889	137.3	132.5	134.2	139.2	138.0	143.5	164.8	147.3	131.6
.667	152.1	153.5	185.7	197.6	212.2	208.3	227.2	191.8	164.8
.500	176.3	188.1	229.4	246.1	265.4	235.9	246.4	176.6	162.6
.389	173.9	190.1	254.4	237.2	264.8	209.7	256.0	181.1	145.1
.222	141.3	147.4	181.1	185.0	163.3	162.4	156.1	146.2	145.9
.111	112.9	121.3	136.7	146.1	140.9	135.4	134.2	129.6	140.1

(h) Mach number

y/y_0	M for z/z_0 of -								
	0.052	0.164	0.276	0.388	0.500	0.612	0.724	0.836	0.948
0.889	1.040	1.038	1.065	1.106	1.093	1.126	1.224	1.122	1.011
.667	1.084	1.176	1.343	1.418	1.445	1.456	1.514	1.327	1.163
.500	1.182	1.256	1.485	1.560	1.608	1.515	1.510	1.210	1.110
.389	1.200	1.315	1.618	1.549	1.650	1.411	1.595	1.230	1.004
.222	1.066	1.138	1.264	1.329	1.225	1.194	1.166	1.102	1.068
.111	.920	.975	1.069	1.142	1.104	1.072	1.053	1.017	1.053

TABLE V.- REDUCED EXPERIMENTAL DATA, CONFIGURATION I, x = 200.7 cm

(a) Fuel mass fraction

y/y_O	$X_{H_2,inj}$ for z/z_O of –								
	0.052	0.164	0.276	0.388	0.500	0.612	0.724	0.836	0.948
1.00	0.037	0.042	0.044	0.043	0.044	0.038	0.037	0.036	0.016
.889	.029	.032	.031	.027	.027	.029	.029	.031	.032
.667	.030	.030	.028	.025	.024	.025	.022	.024	.018
.500	.034	.031	.027	.022	.021	.024	.024	.028	.031
.389	.040	.038	.036	.035	.033	.036	.035	.033	.035
.222	.043	.040	.040	.040	.038	.040	.038	.035	.034
.111	.040	.049	.047	.048	.045	.042	.038	.039	.039
0	.053	.049	.050	.052	.053	.054	.052	.048	.045

(b) Reacted fuel mass fraction

y/y_O	$X_{H_2,R}$ for z/z_O of –								
	0.052	0.164	0.276	0.388	0.500	0.612	0.724	0.836	0.948
1.00	0.027	0.028	0.028	0.028	0.028	0.027	0.027	0.027	0.016
.889	.026	.027	.027	.024	.024	.025	.026	.027	.027
.667	.026	.027	.025	.023	.022	.023	.021	.022	.017
.500	.027	.027	.024	.020	.020	.022	.022	.025	.027
.389	.028	.027	.027	.027	.027	.027	.027	.027	.027
.222	.028	.028	.027	.028	.027	.027	.027	.027	.027
.111	.028	.029	.029	.029	.028	.028	.027	.027	.027
0	.029	.029	.029	.029	.029	.030	.029	.029	.028

TABLE V.- Continued

(c) Nondimensional measured pitot pressure

y/y$_o$	$P_{t,2}/P_{t,h}$ for z/z$_o$ of -								
	0.052	0.164	0.276	0.388	0.500	0.612	0.724	0.836	0.948
1.00	0.081	0.090	0.099	0.104	0.094	0.102	0.105	0.083	0.090
.889	.092	.108	.132	.160	.149	.167	.158	.121	.096
.667	.099	.117	.140	.161	.153	.164	.157	.117	.090
.500	.093	.109	.131	.158	.147	.152	.140	.113	.090
.389	.090	.111	.111	.116	.119	.126	.116	.082	.088
.222	.080	.089	.095	.099	.098	.094	.091	.089	.078
.111	.061	.061	.061	.061	.061	.061	.061	.061	.061
0	.061	.061	.061	.061	.061	.061	.061	.061	.061

(d) Nondimensional corrected pitot pressure

y/y$_o$	$(P_{t,2}/P_{t,h})_{corr}$ for z/z$_o$ of -								
	0.052	0.164	0.276	0.388	0.500	0.612	0.724	0.836	0.948
1.00	0.094	0.099	0.106	0.111	0.101	0.111	0.114	0.096	0.091
.889	.100	.116	.139	.164	.154	.173	.164	.129	.105
.667	.107	.124	.146	.165	.157	.168	.160	.121	.092
.500	.103	.117	.136	.160	.149	.155	.143	.119	.099
.389	.099	.119	.120	.125	.128	.135	.125	.095	.100
.222	.090	.098	.104	.107	.107	.103	.101	.100	.094
.111	.215	.137	.150	.142	.166	.200	.243	.232	.227
0	.105	.133	.130	.116	.109	.101	.114	.146	.165

TABLE V.- Continued

(e) Velocity

y/y₀	V, m/sec, for z/z₀ of -								
	0.052	0.164	0.276	0.388	0.500	0.612	0.724	0.836	0.948
1.00	1055	1123	1196	1240	1157	1223	1241	1073	896
.889	1091	1252	1404	1497	1443	1558	1517	1337	1162
.667	1168	1299	1412	1478	1426	1500	1421	1221	922
.500	1145	1259	1347	1421	1359	1419	1365	1240	1092
.389	1121	1285	1285	1317	1336	1385	1320	1057	1114
.222	1029	1114	1165	1199	1192	1161	1132	1118	1043
.111	1789	1444	1520	1475	1596	1736	1878	1843	1829
0	1216	1423	1403	1310	1255	1184	1296	1496	1595

(f) Static temperature

y/y₀	T, K, for z/z₀ of -								
	0.052	0.164	0.276	0.388	0.500	0.612	0.724	0.836	0.948
1.00	3049	3015	2991	2999	2990	3046	3056	3066	2749
.889	3117	3167	3164	3077	3071	3120	3121	3160	3154
.667	3140	3147	3099	3032	2999	3042	2954	3001	2823
.500	3107	3163	3077	2949	2926	2999	3019	3093	3145
.389	3024	3044	3066	3075	3119	3065	3071	3136	3074
.222	3004	3024	3030	3025	3045	3026	3046	3071	3075
.111	3039	2959	2974	2965	2991	3025	3066	3055	3051
0	2922	2955	2952	2936	2927	2917	2933	2969	2991

TABLE V.- Concluded

(g) Mass flux

y/y_0	ρV, kg/m²-sec, for z/z_0 of -								
	0.052	0.164	0.276	0.388	0.500	0.612	0.724	0.836	0.948
1.00	116.7	122.6	130.2	136.9	124.9	139.0	142.5	120.3	127.7
.889	128.3	146.2	170.3	199.8	190.5	204.8	196.7	160.1	133.3
.667	136.9	155.9	180.9	203.0	197.3	205.8	202.8	159.8	126.4
.500	131.0	147.7	172.5	203.5	194.0	196.0	183.1	152.9	125.7
.389	123.2	147.7	150.0	155.7	158.8	165.2	155.8	119.0	126.5
.222	109.7	122.2	129.6	133.8	134.7	128.7	126.5	126.8	117.2
.111	233.0	161.7	175.2	167.0	189.7	220.0	256.7	247.1	243.4
0	126.5	158.0	154.8	140.1	132.0	122.0	138.0	170.7	189.5

(h) Mach number

y/y_0	M for z/z_0 of -								
	0.052	0.164	0.276	0.388	0.500	0.612	0.724	0.836	0.948
1.00	0.892	0.942	1.002	1.045	0.965	1.047	1.068	0.914	0.857
.889	.952	1.089	1.244	1.389	1.332	1.435	1.388	1.177	1.002
.667	1.018	1.145	1.284	1.390	1.346	1.410	1.361	1.122	.866
.500	.985	1.097	1.225	1.364	1.302	1.338	1.269	1.107	.943
.389	.944	1.106	1.116	1.150	1.171	1.215	1.152	.903	.955
.222	.853	.937	.987	1.017	1.018	.982	.962	.957	.889
.111	1.635	1.224	1.307	1.257	1.393	1.565	1.758	1.709	1.689
0	.994	1.201	1.181	1.085	1.031	.963	1.071	1.280	1.392

Mach 2.7 nozzle

Flow

Water cooled

6.4°

3.35°

4.57°

Step injector (uncooled)

Uncooled model

Pitot/Sample probe survey locations

Engine combuster side wall
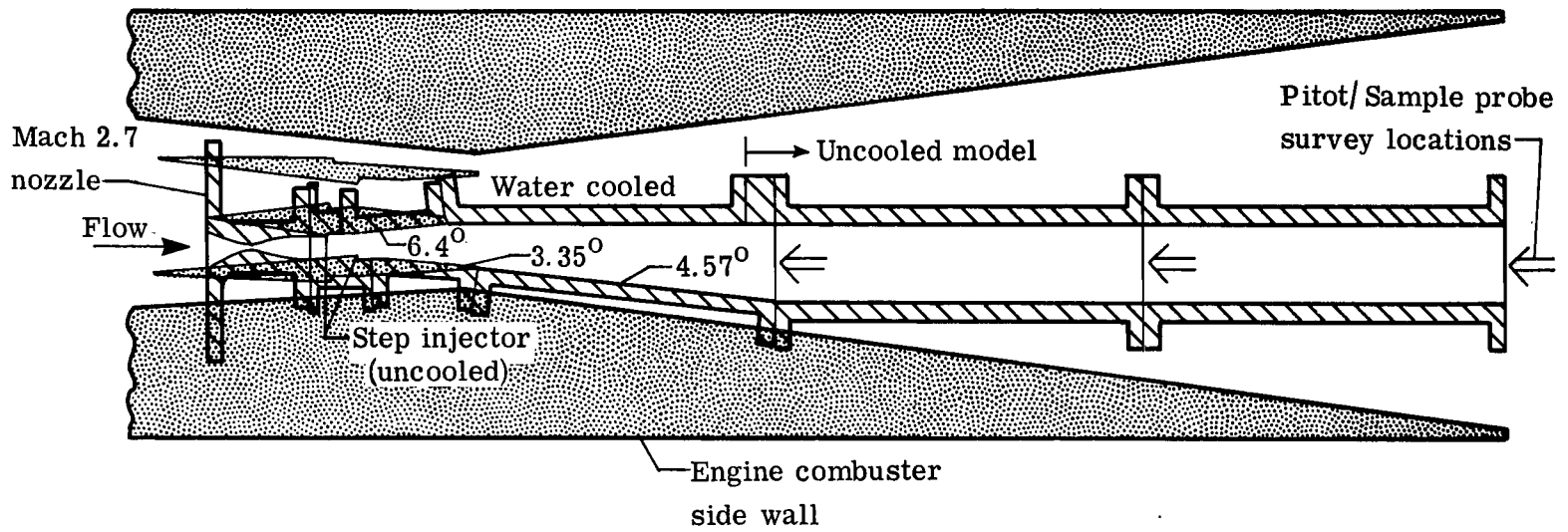
(a) Scramjet module combustor simulation.

Figure 1.- Combustor model.

V

⊙

⊙

2.12

Top wall

⊙

⊙

2.54 ← 4.70 →

.381 →

h_t

3.84 - 4.24 - 4.29
4.67

h_b

z

.381 →
2.159 →

Bottom wall

⊙
4.24

⊙
y
4.24

x
2.12
⊙
4.24

⊙

2.54 ← 5.08 →
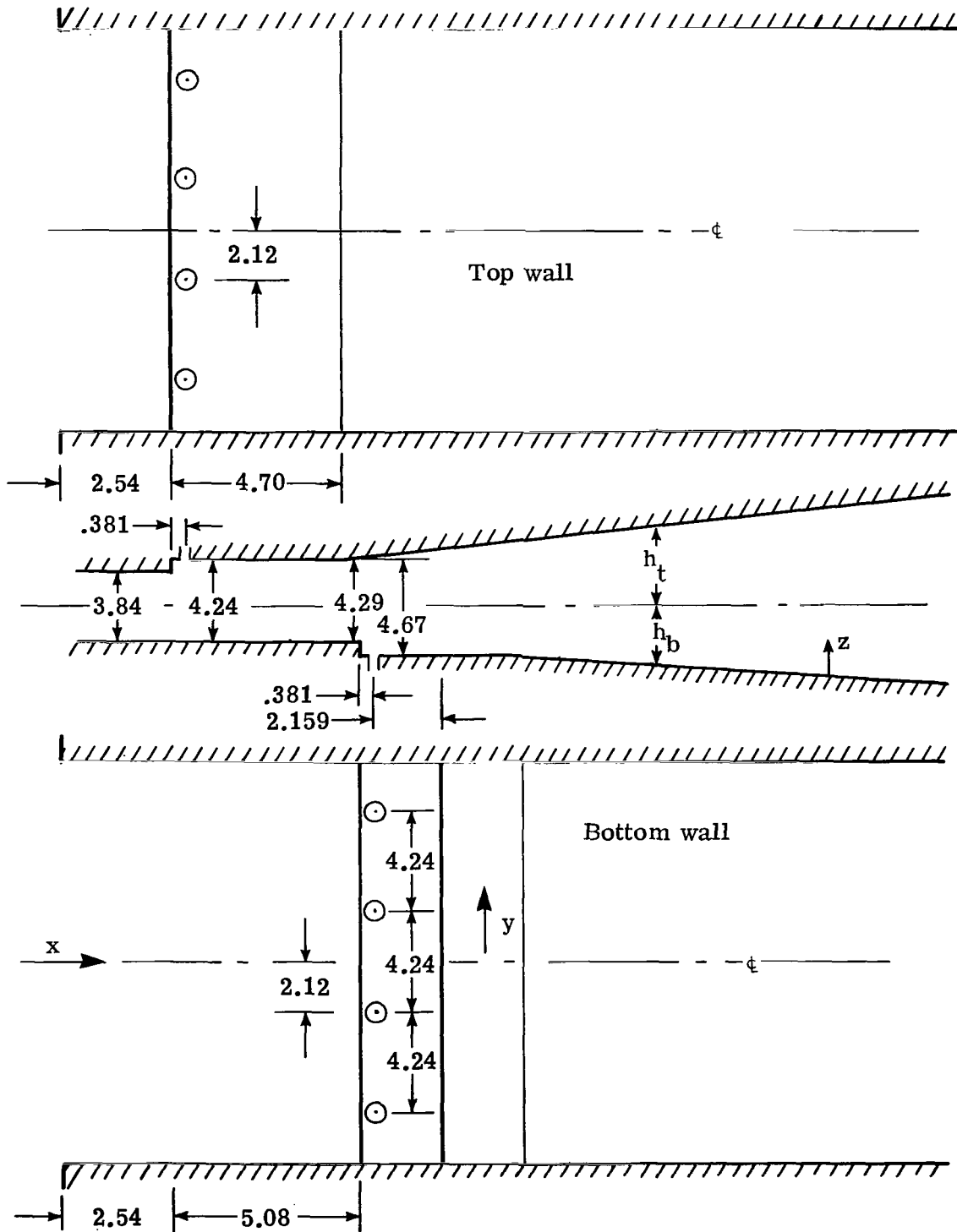
(b) Injector detail. All injectors are 0.295 cm in diameter.
All dimensions are in centimeters.

Figure 1.- Concluded.

Cooling water

Duct
side
walls

9 probes,
1.905 cm
spacing

Rake
strut

Cooling
water

Probe tip detail

Cooling water
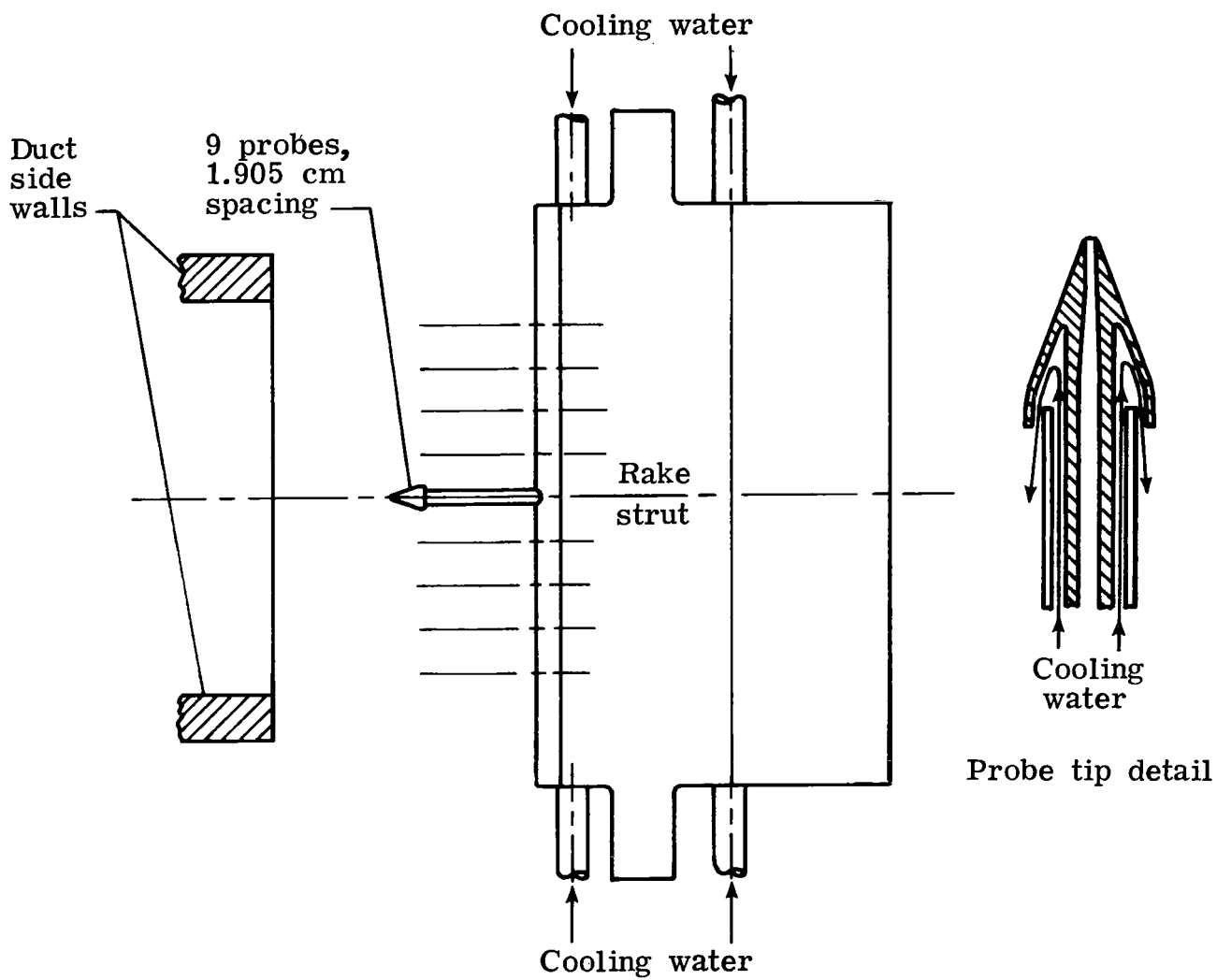
Figure 2.- Sketch of pitot-pressure gas sample probe rake.
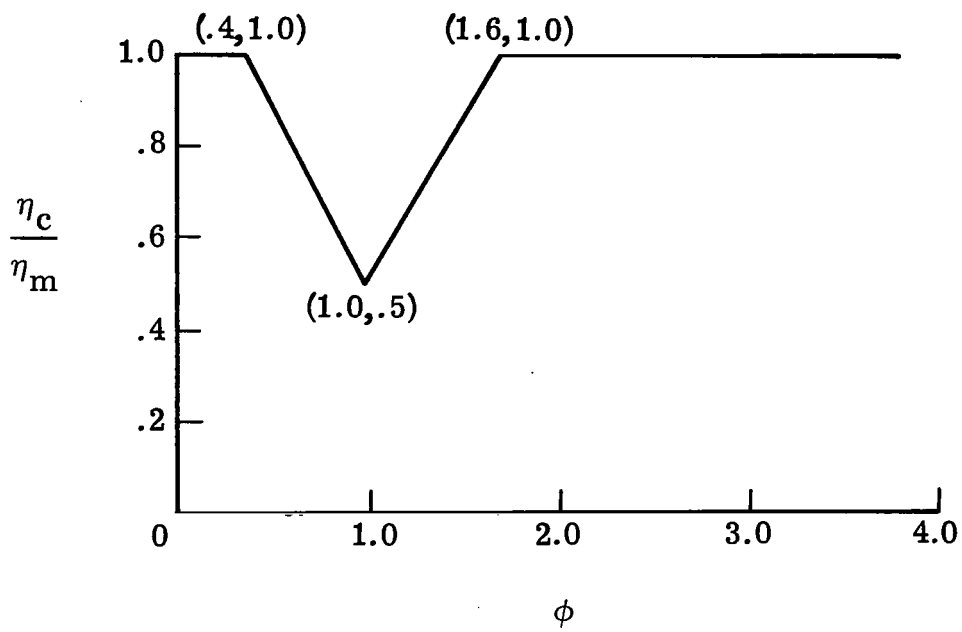
Figure 3.- Empirical combustion efficiency model.
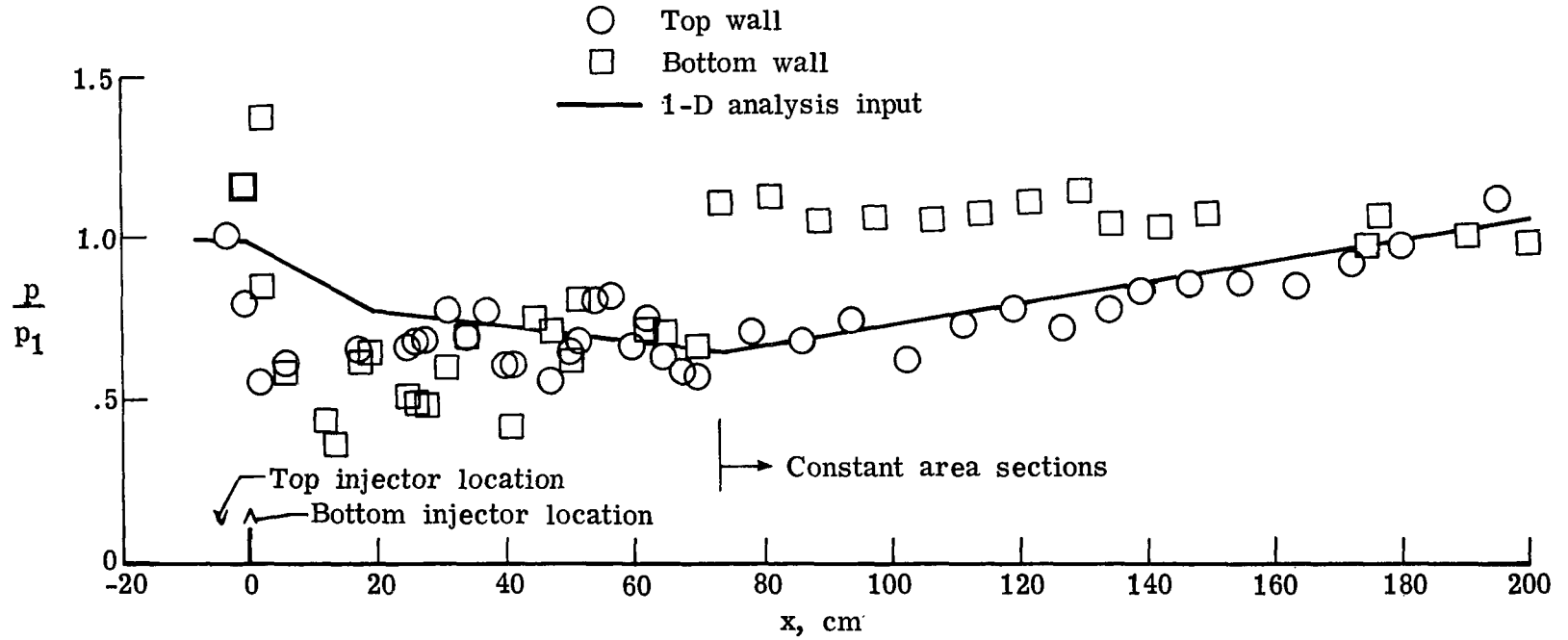
(a) Configuration I; $\phi_T + \phi_B = 0.97$.

Figure 4.- Combustor wall pressure.
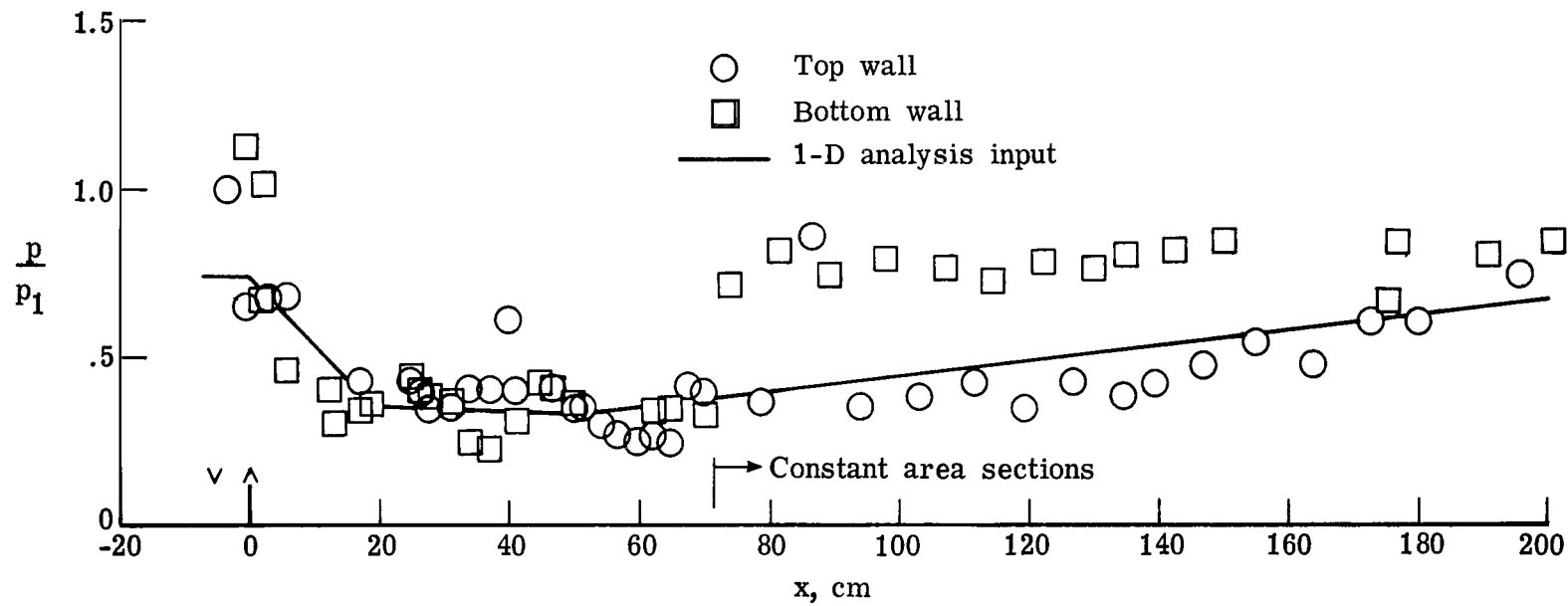
(b) Configuration II; $\phi_B = 0.47$.

Figure 4.- Continued.
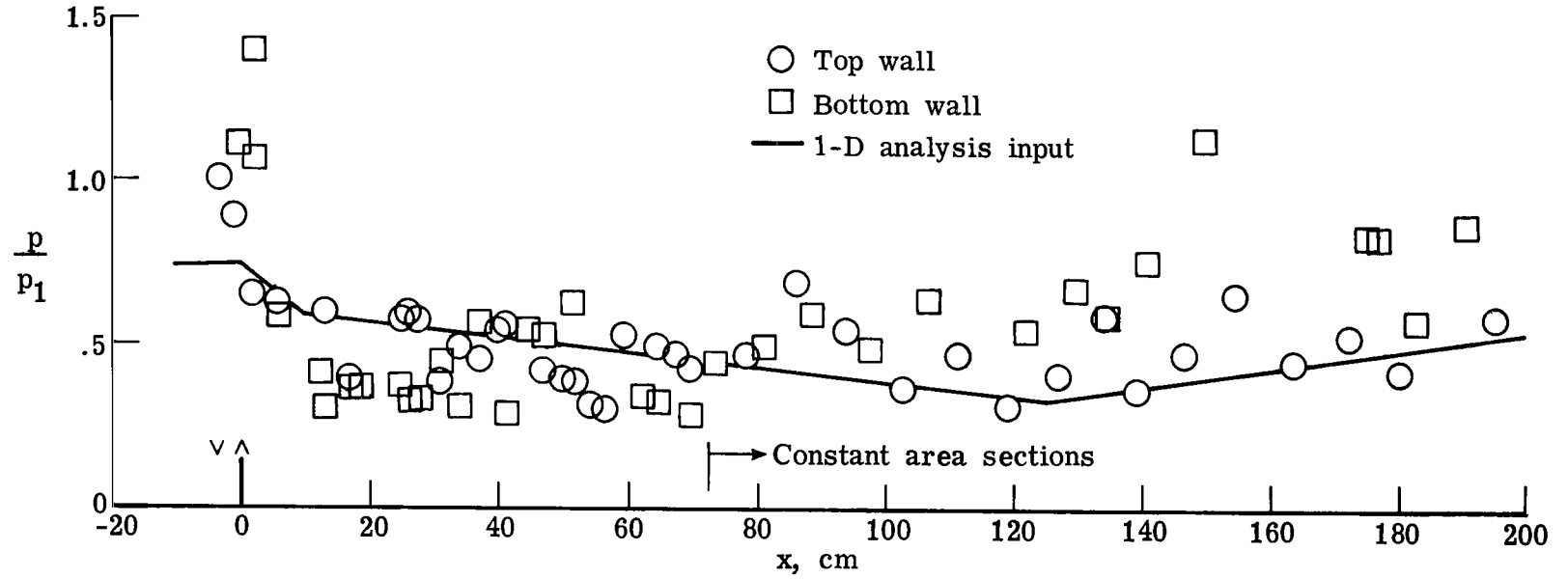
(c) Configuration III; $\phi_T = 0.51$.

Figure 4.- Concluded.
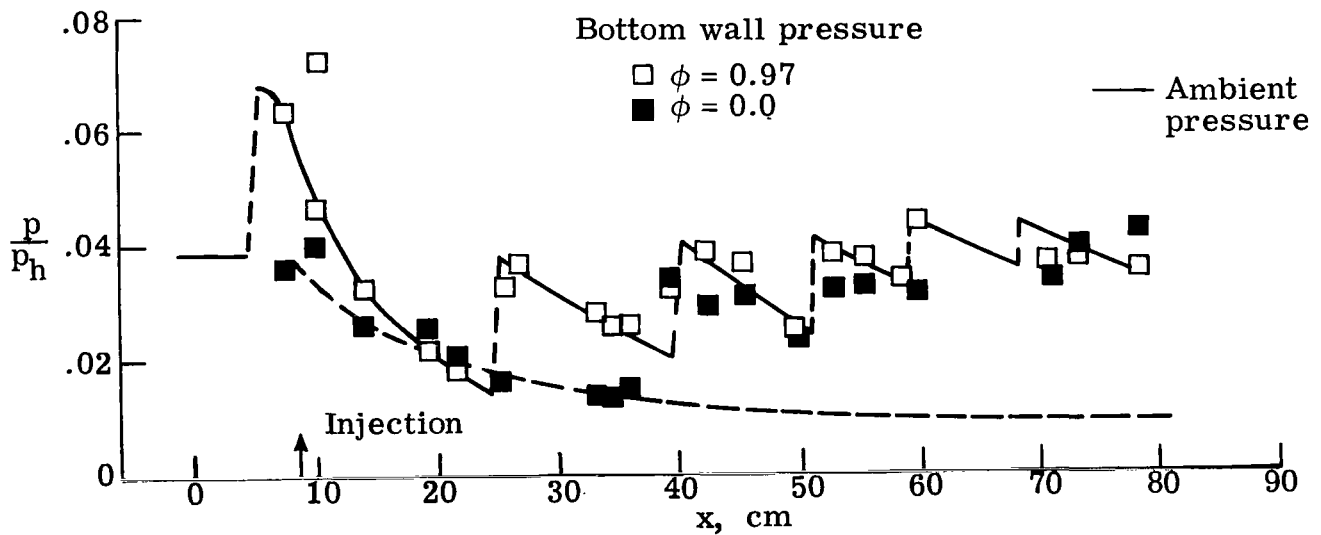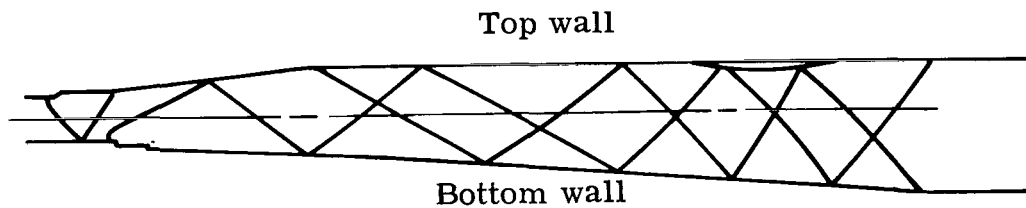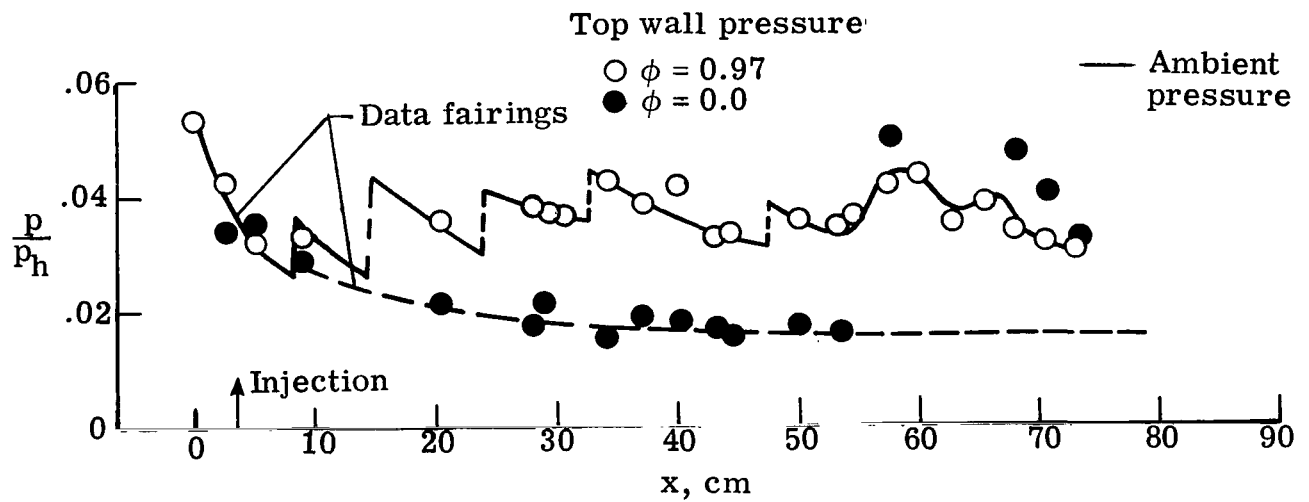
(a) Configuration I; $\phi = 0.97$.

Figure 5.- Wall pressure and shock diagram in diverging section.
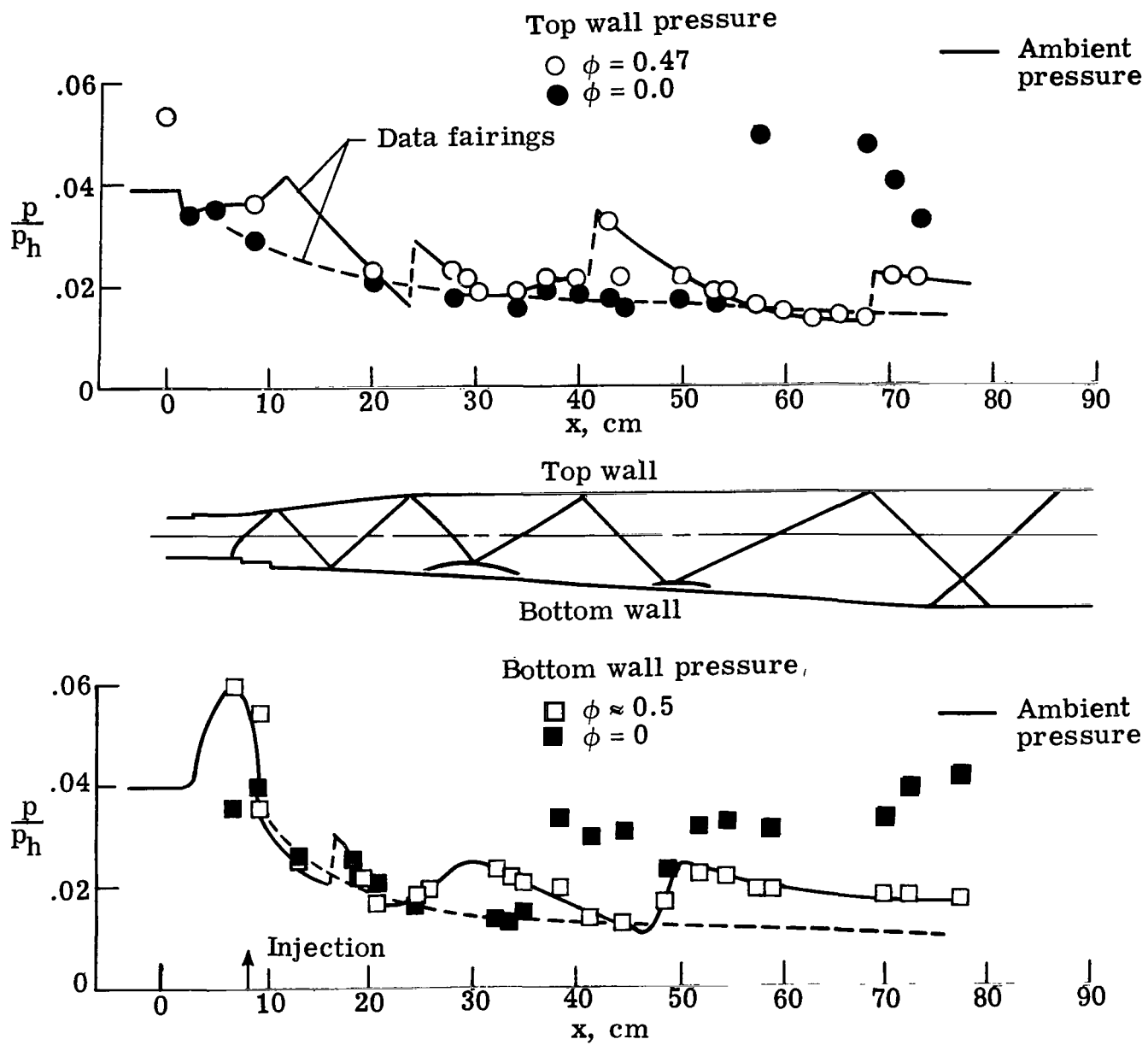
(b) Configuration II; $\phi_B = 0.47$.

Figure 5.- Continued.

Top wall pressure
○ $\phi = 0.51$
● $\phi = 0.0$
—— Ambient pressure

Data fairing

Bottom wall pressure
□ $\phi = 0.51$
■ $\phi = 0.0$
—— Ambient pressure
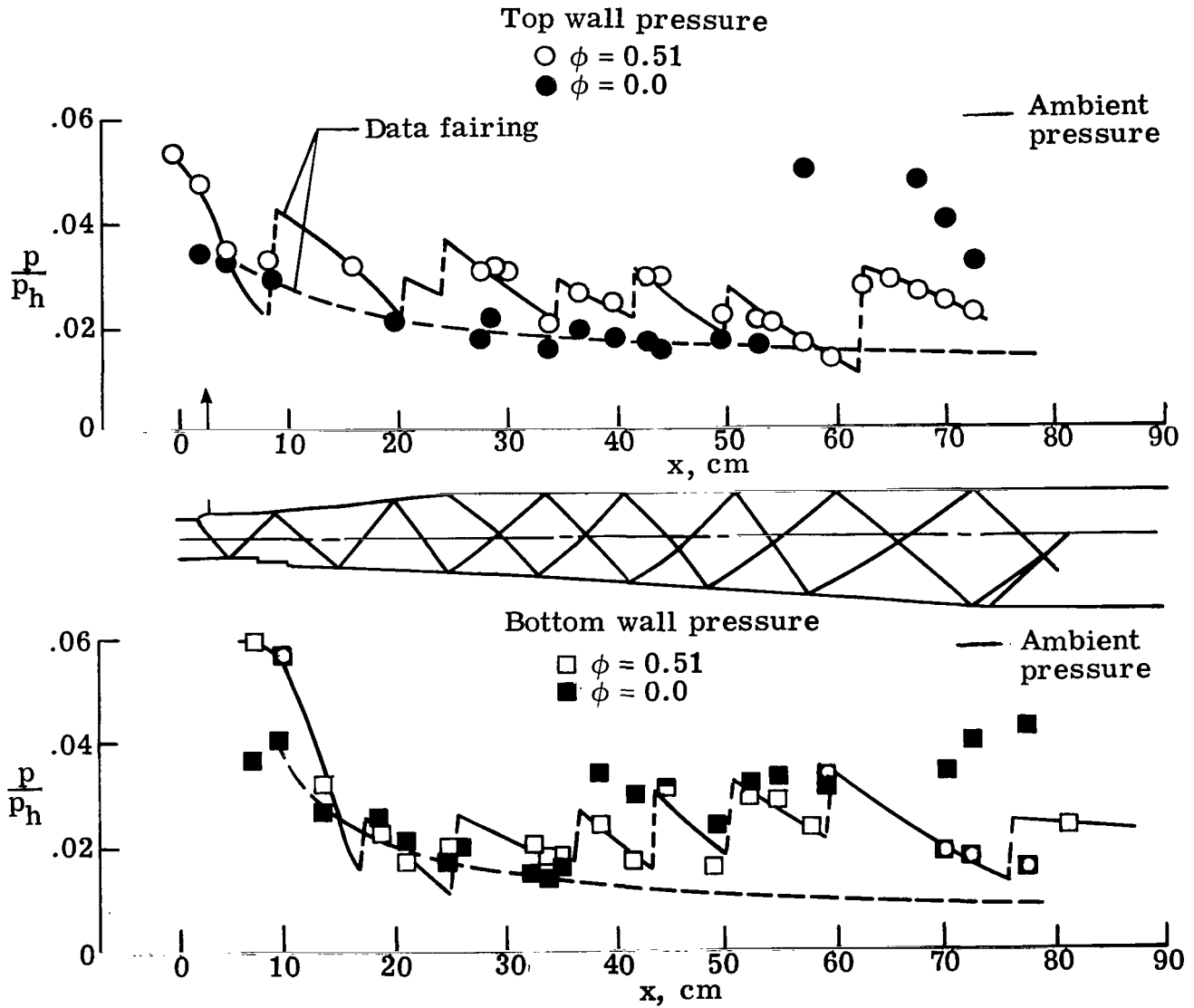
(c) Configuration III; $\phi_T = 0.51$.

Figure 5.- Concluded.
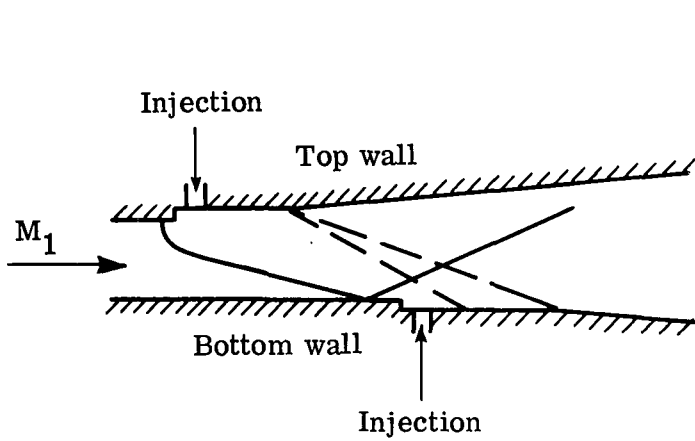
(a) Top-wall induced shock.
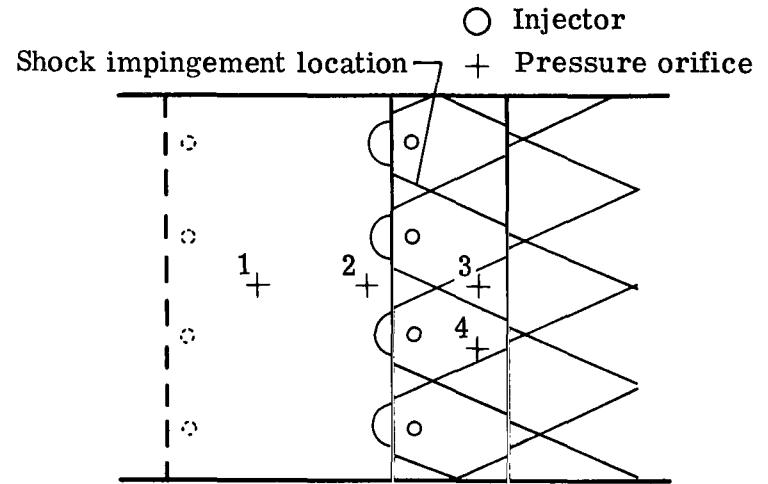
(b) Shock impingement.
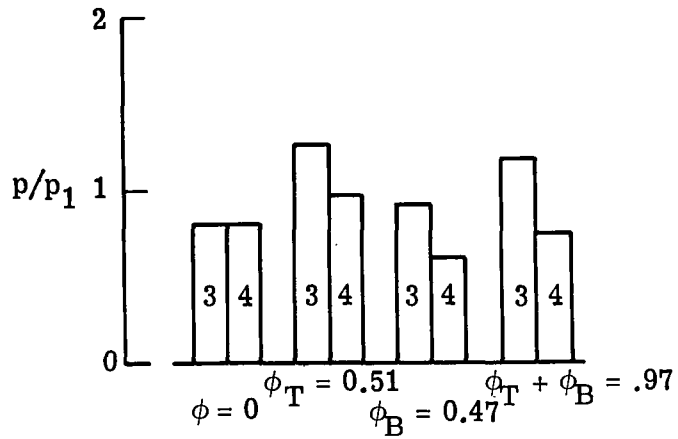
(c) Nondimensional wall pressure.
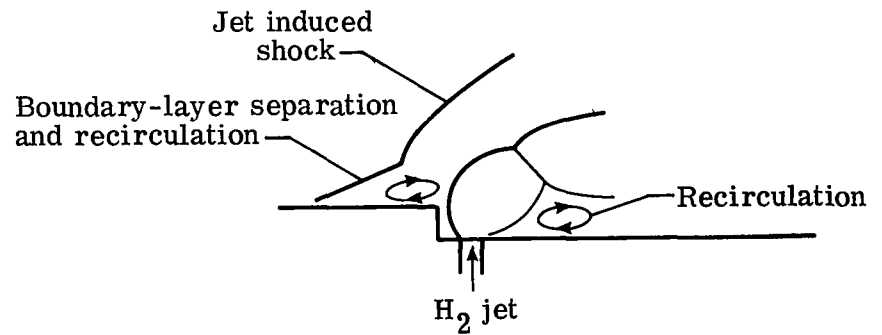
(d) Jet-flow interaction detail.

Figure 6.- Flow details in vicinity of fuel jets.
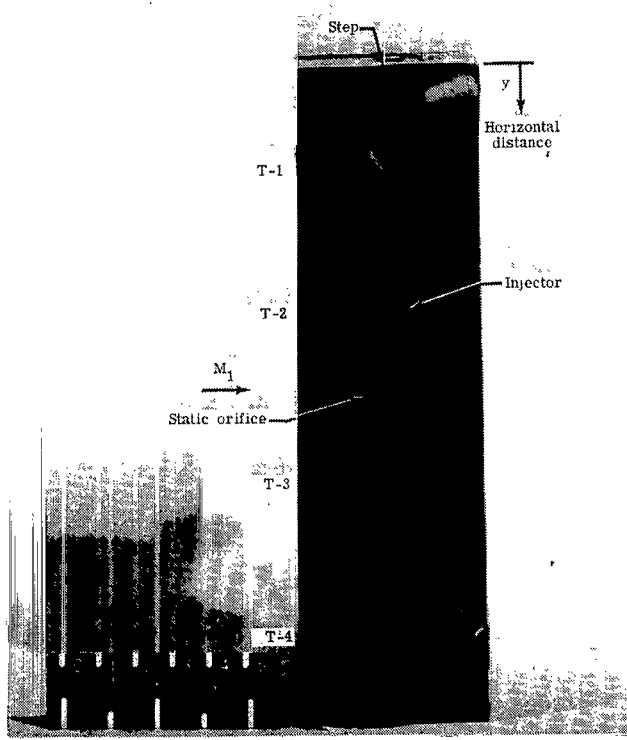
(a) Top wall. L-76-3250.1
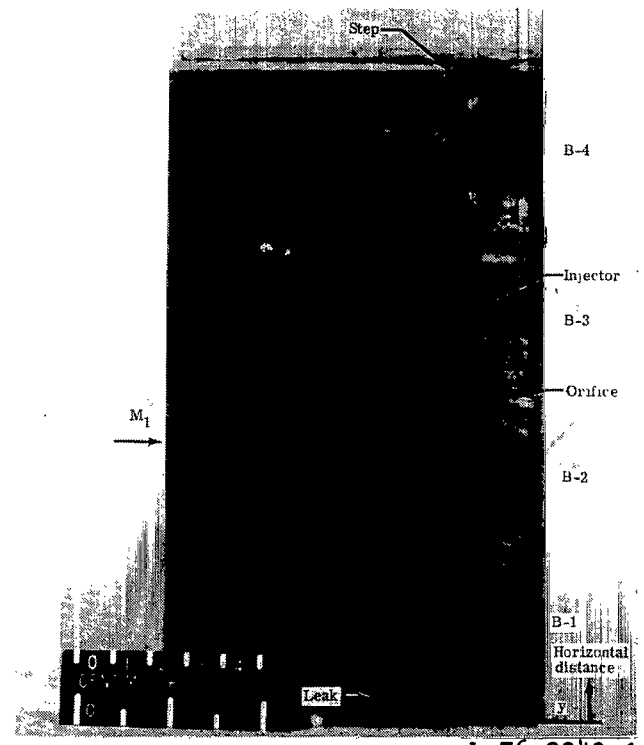
(b) Bottom wall. L-76-3249.1

Figure 7.- Injector block heating pattern.
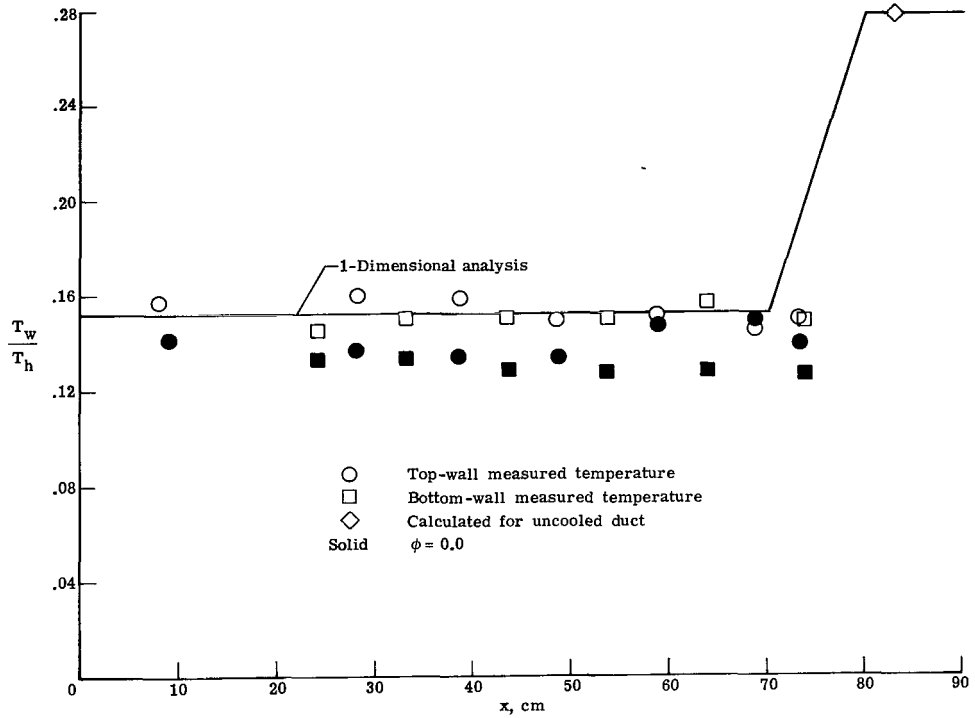
(a) Configuration I; φ = 0.97.
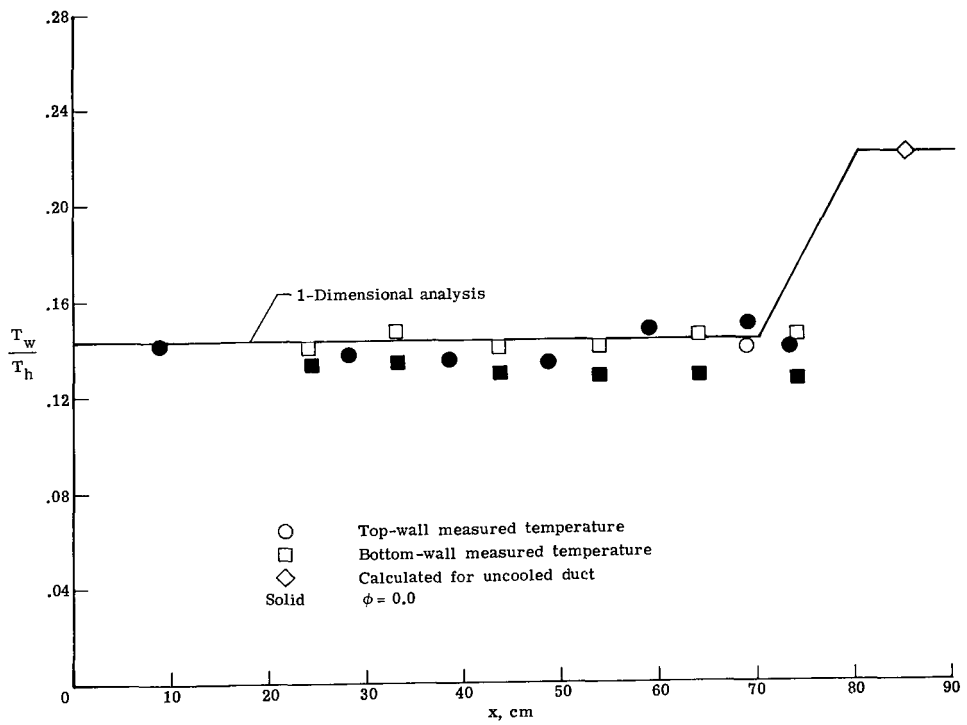
(b) Configuration II; ϕ_B = 0.47.

Figure 8.- Nondimensional combustor wall temperature.

.28

.24

.20

.16

$\dfrac{T_w}{T_h}$

.12

.08

○ Top-wall measured temperature
□ Bottom-wall measured temperature
◇ Calculated for uncooled duct
Solid $\phi = 0.0$

.04

0   10   20   30   40   50   60   70   80   90

x, cm
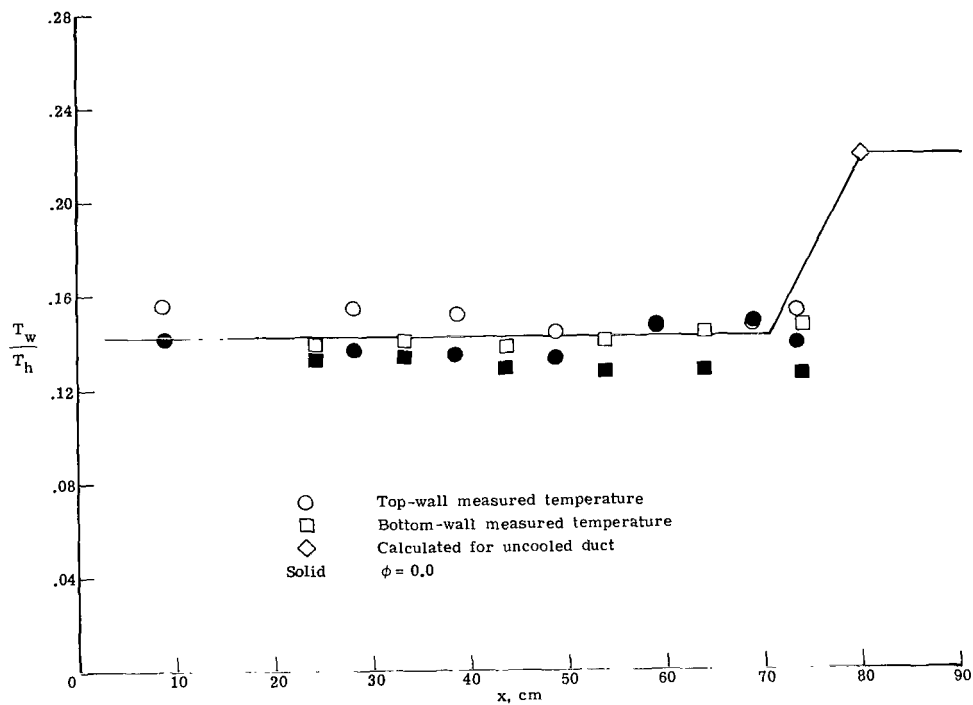
(c) Configuration III; $\phi_T = 0.51$.

Figure 8.- Concluded.
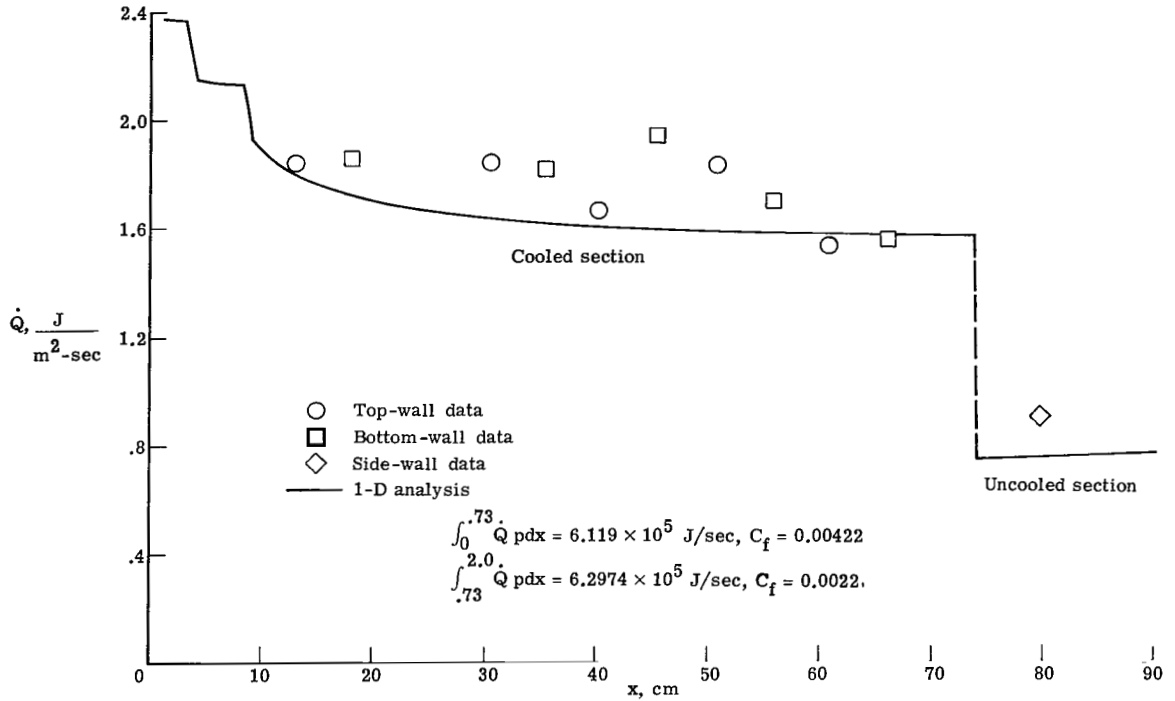
(a) Configuration I; ϕ = 0.97.
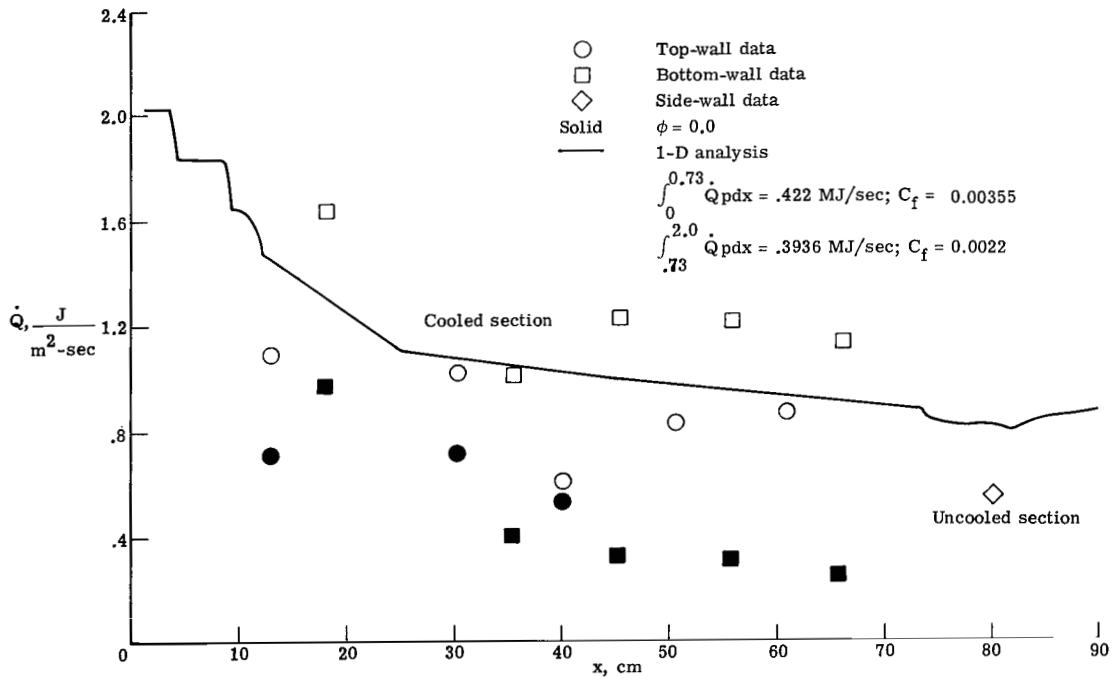
(b) Configuration II; ϕ_B = 0.47.

Figure 9.- Combustor wall heat flux.
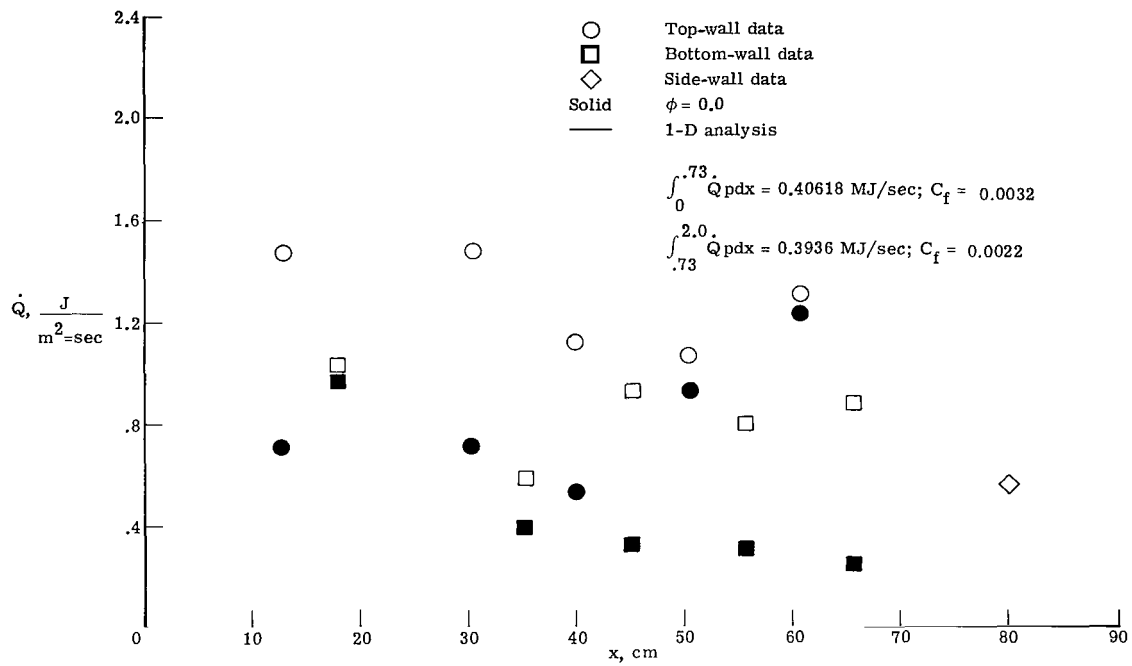
(c) Configuration III; $\phi_T = 0.51$.

Figure 9.- Concluded.
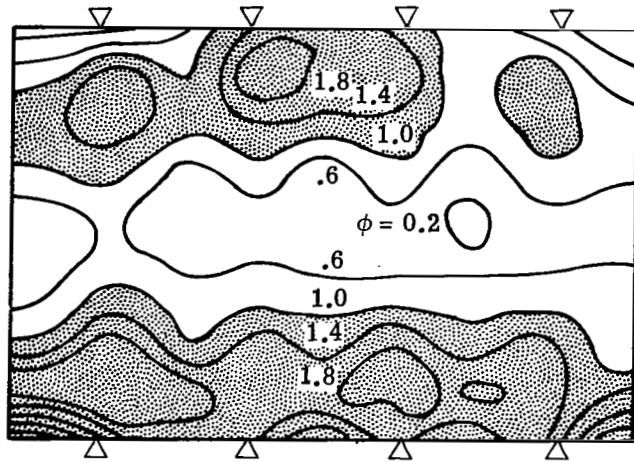
(a) First duct exit; x = 78.7 cm.
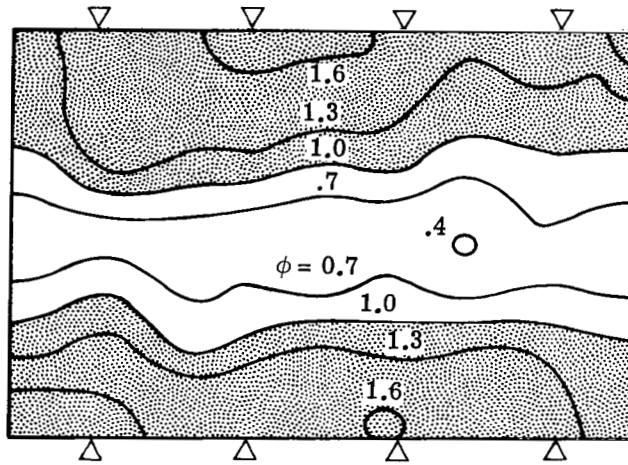
(b) Second duct exit; x = 139.7 cm.
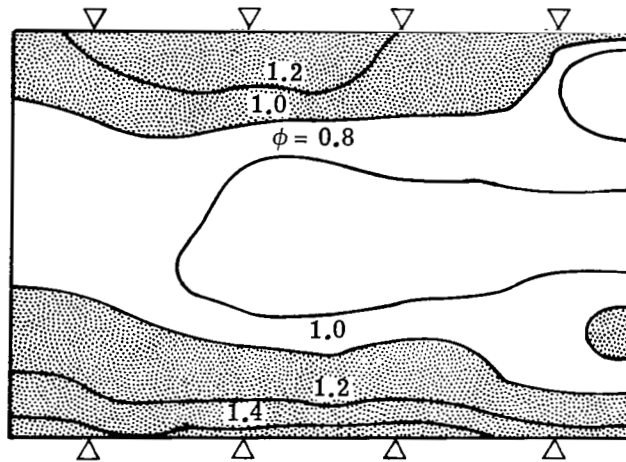
(c) Third duct exit; x = 200.7 cm.

Figure 10.- Equivalence ratio contours. Configuration I; ϕ = 0.97.
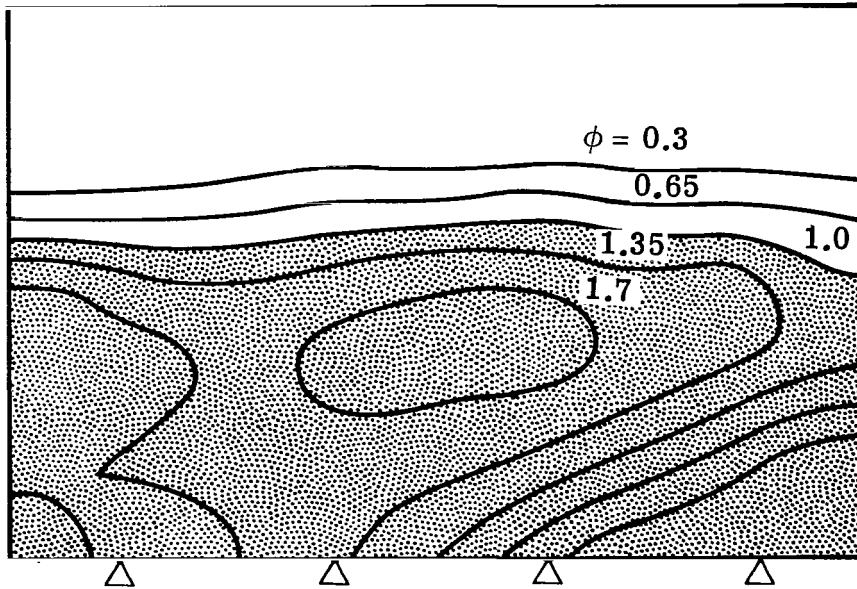
(a) First duct exit; x = 78.7 cm.
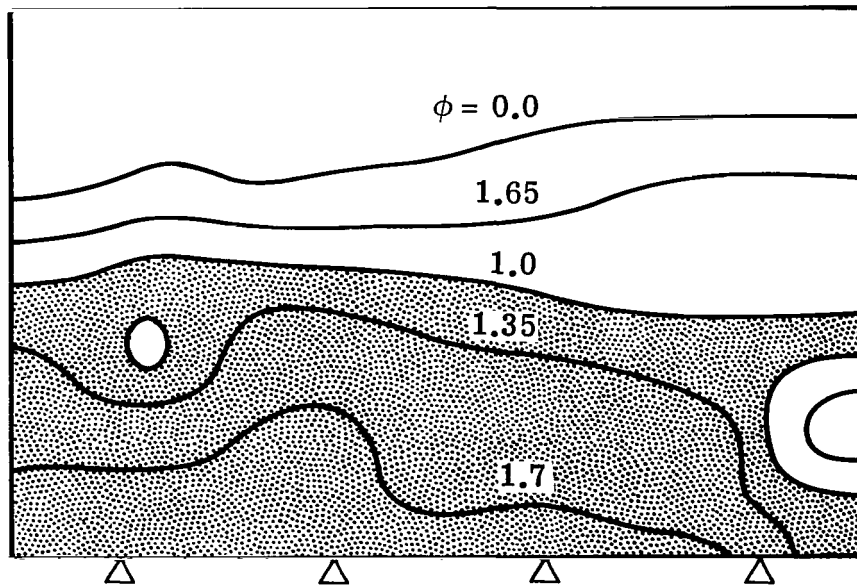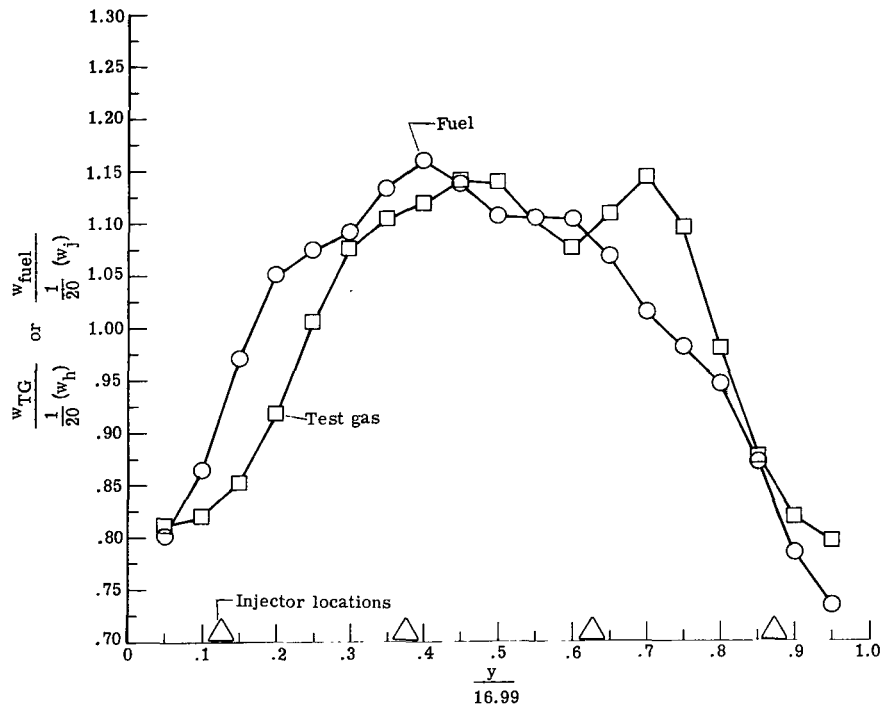

(b) Third duct exit; x = 200.7 cm.

Figure 11.- Equivalence ratio contours. Configuration II; ϕ_B = 0.47.
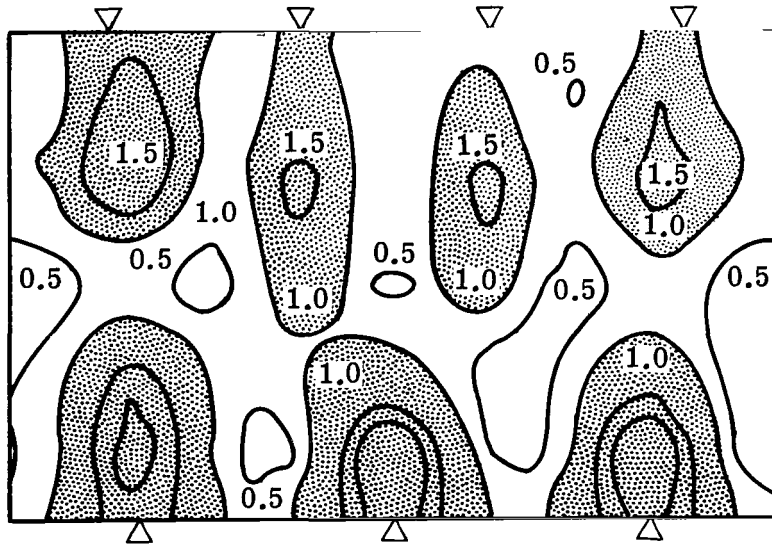
Figure 12.- Equivalence ratio contours (ref. 12). Configuration Q_3; $\phi = 0.89$; first duct exit; x = 78.7 cm.
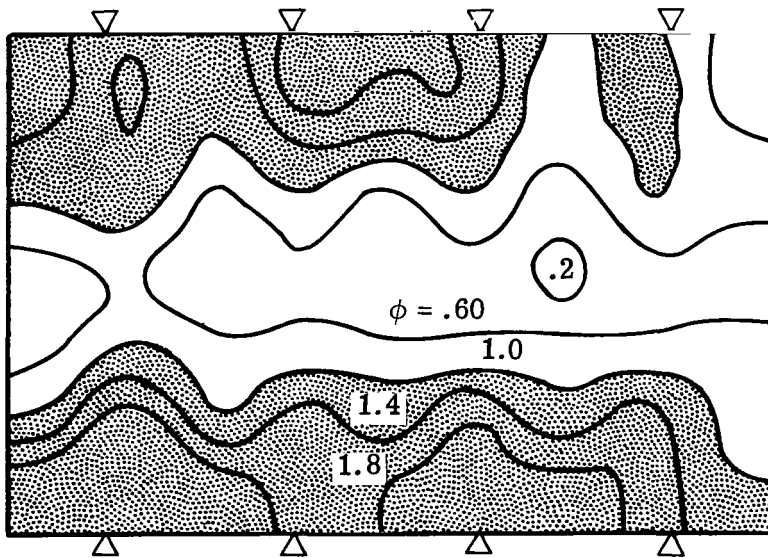
Figure 13.- Reflection plane method equivalence ratio contours. Configuration I; $\phi = 0.97$; first duct exit; x = 78.7 cm; $w_j = 0.09378$ kg/sec by wall concentration method; $w_j = 0.09164$ kg/sec by reflection method.
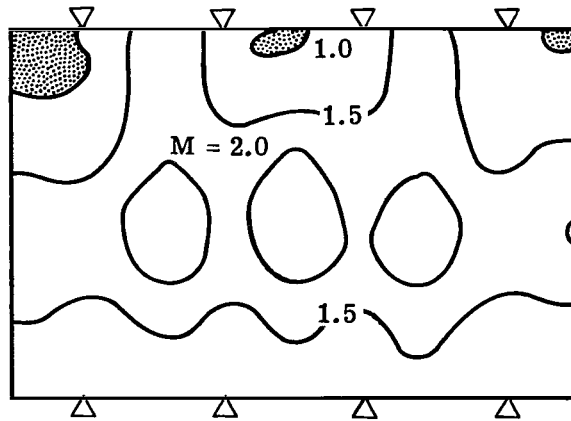
(a) First duct exit; x = 78.7 cm; $\bar{M}$ = 1.612.
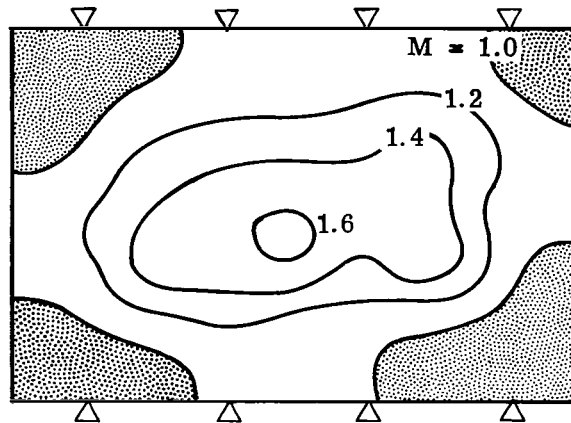
(b) Second duct exit; x = 139.7 cm; $\bar{M}$ = 1.430.
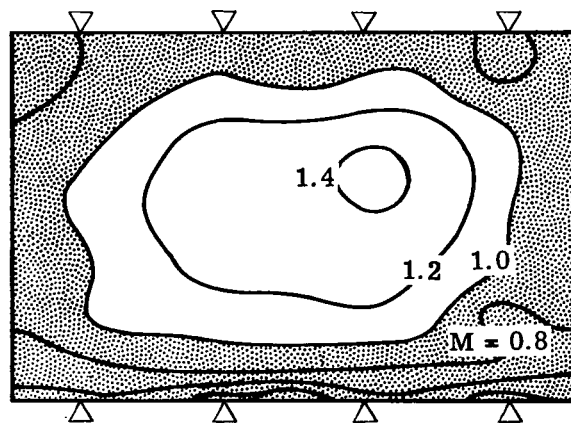
(c) Third duct exit; x = 200.7 cm; $\bar{M}$ = 1.243.

Figure 14.- Mach number contours. Configuration I; ϕ = 0.97.
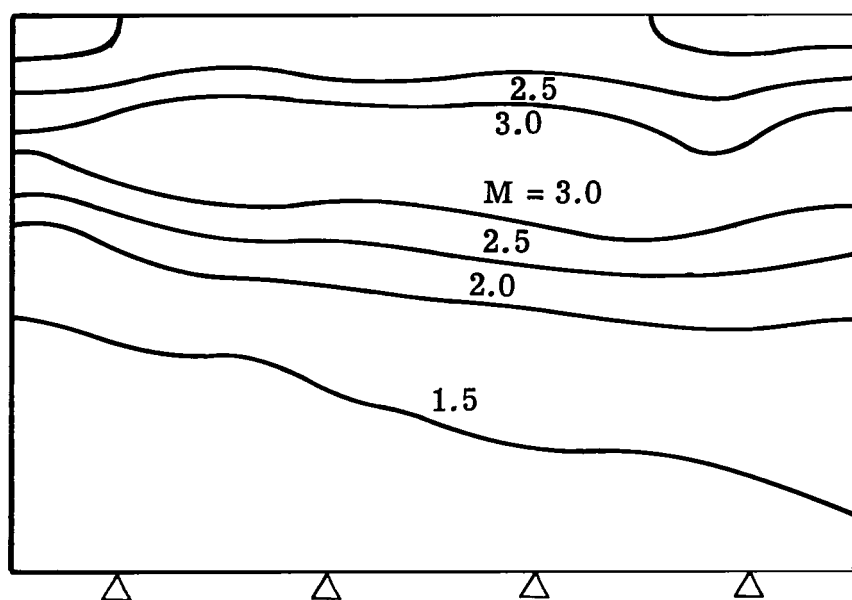
(a) First duct exit; x = 78.7 cm; $\bar{M}$ = 2.180.
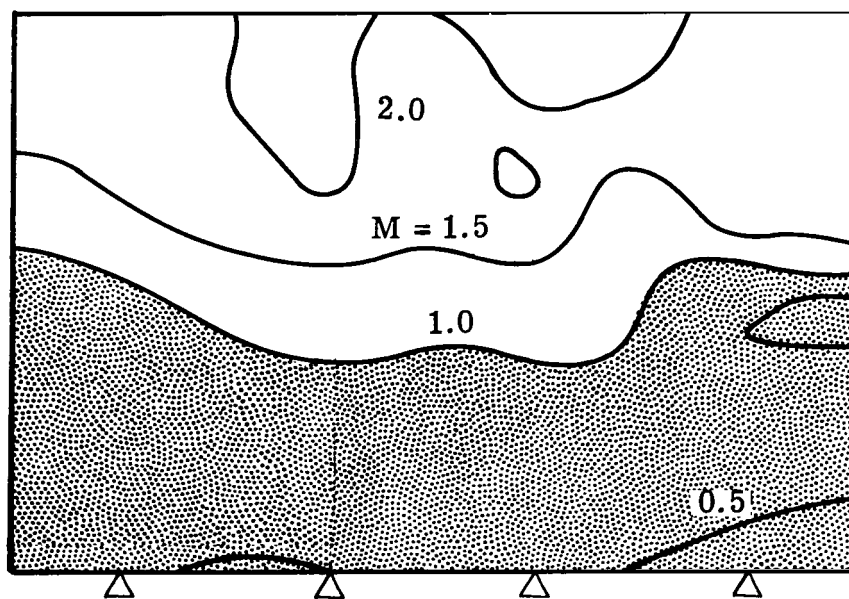
(b) Third duct exit; x = 200.7 cm; $\bar{M}$ = 1.426.

Figure 15.- Mach number contours. Configuration II; ϕ_B = 0.47.
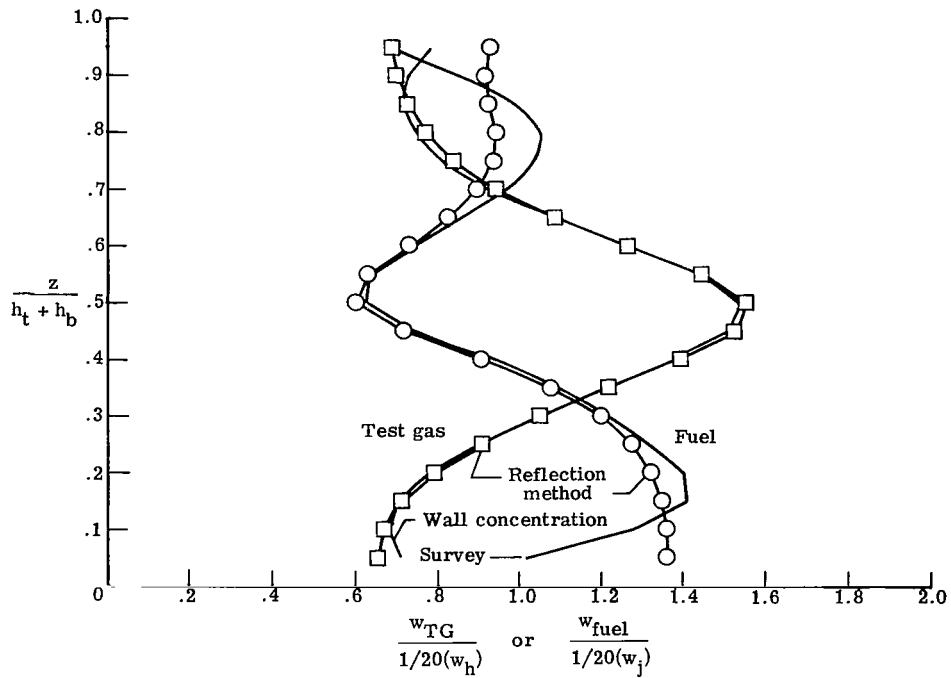
(a) Configuration I; $\phi = 0.97$; first duct exit.
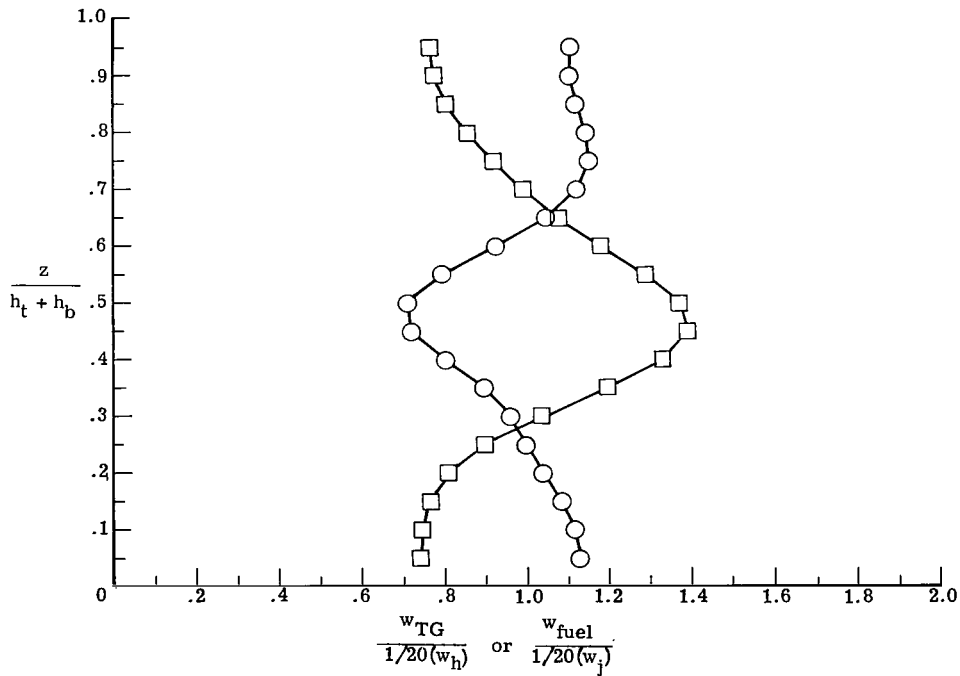
(b) Configuration I; $\phi = 0.97$; second duct exit; no wall concentration data for this case.

Figure 16.- Vertical distribution of fuel and test gas.
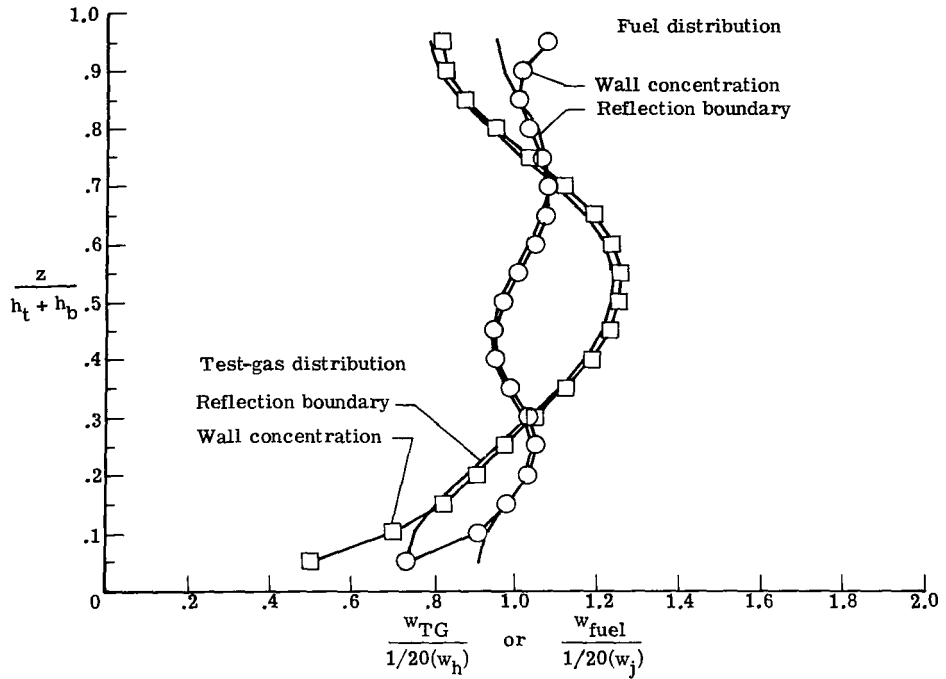
(c) Configuration I; third duct exit; ϕ = 0.97.
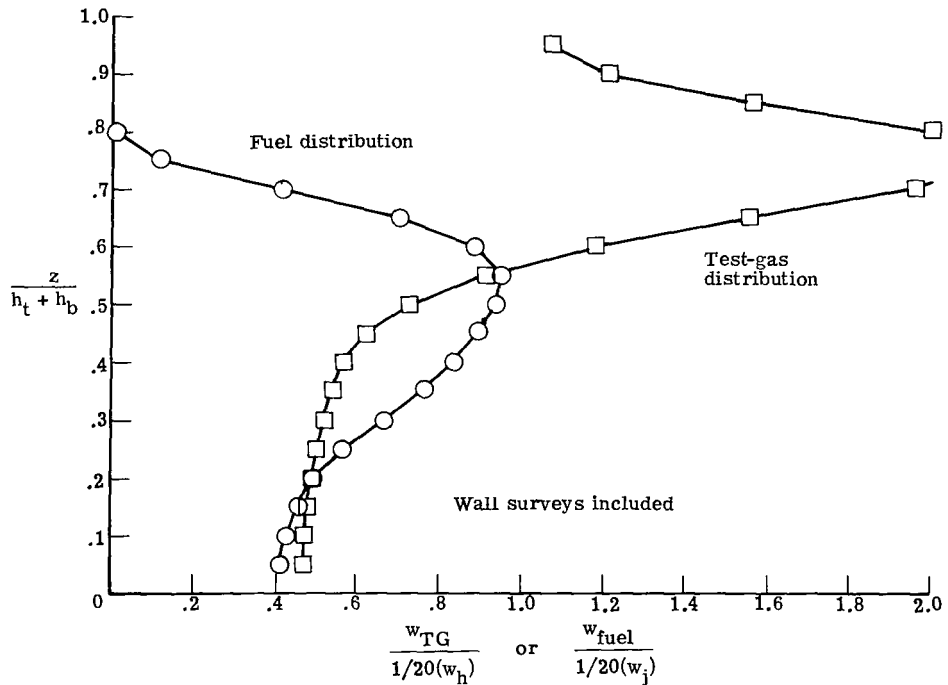
(d) Configuration II; ϕ_B = 0.47; first duct exit.

Figure 16.- Continued.
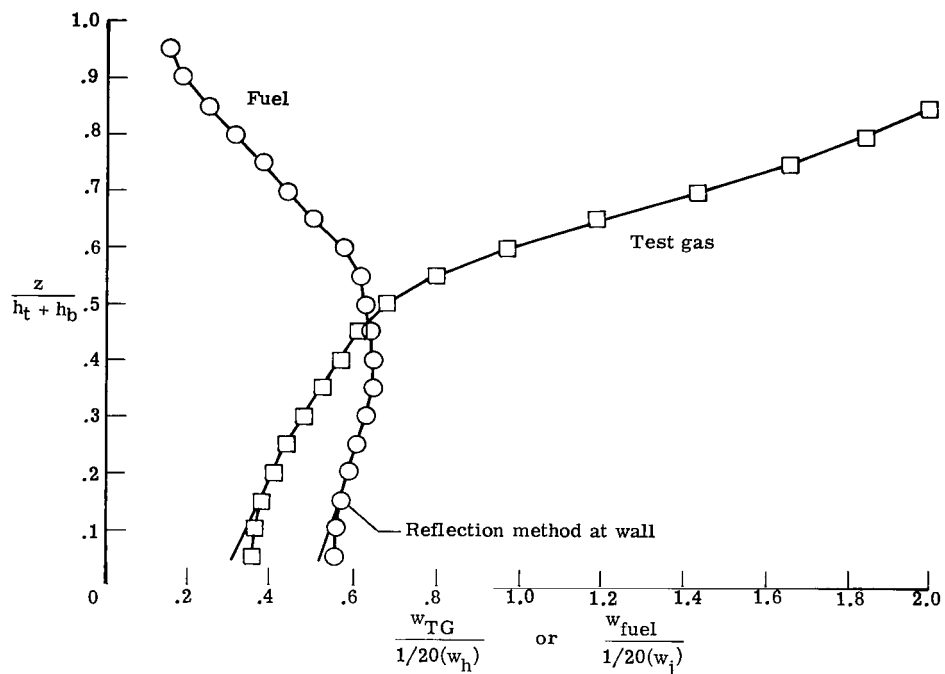
(e) Configuration II; ϕ_B = 0.47; third duct exit.

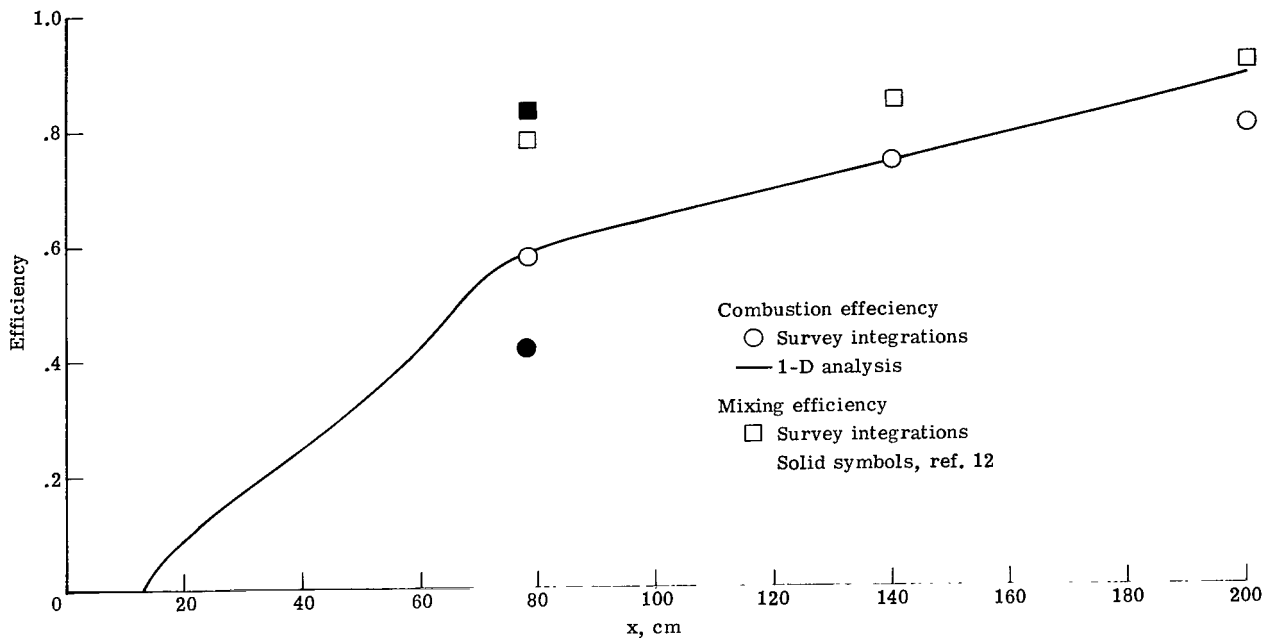Figure 16.- Concluded.
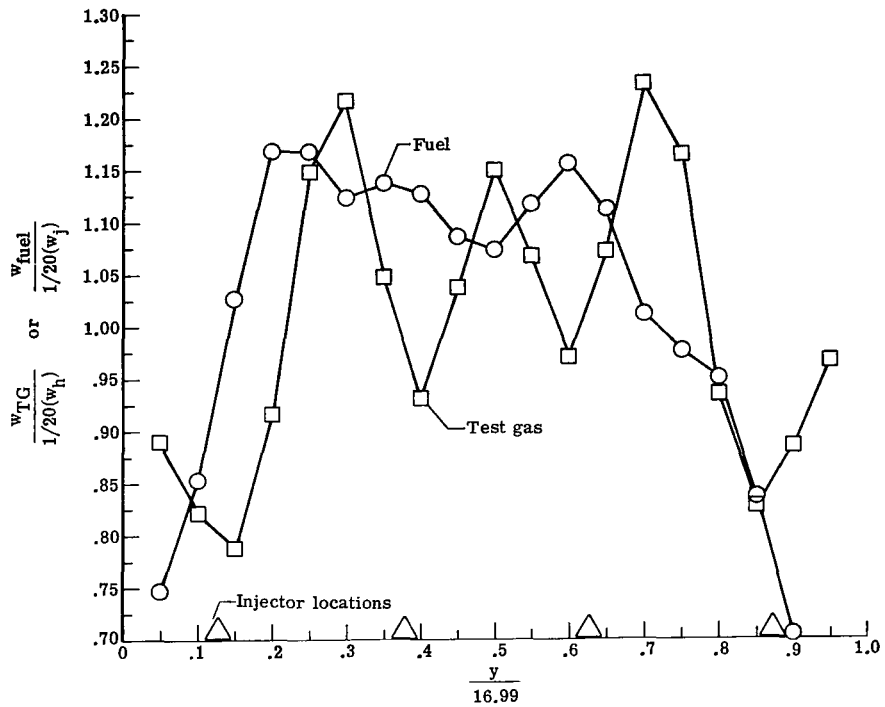
(a) First duct exit;   x = 78.7 cm.

(b) Second duct exit;   x = 139.7 cm.

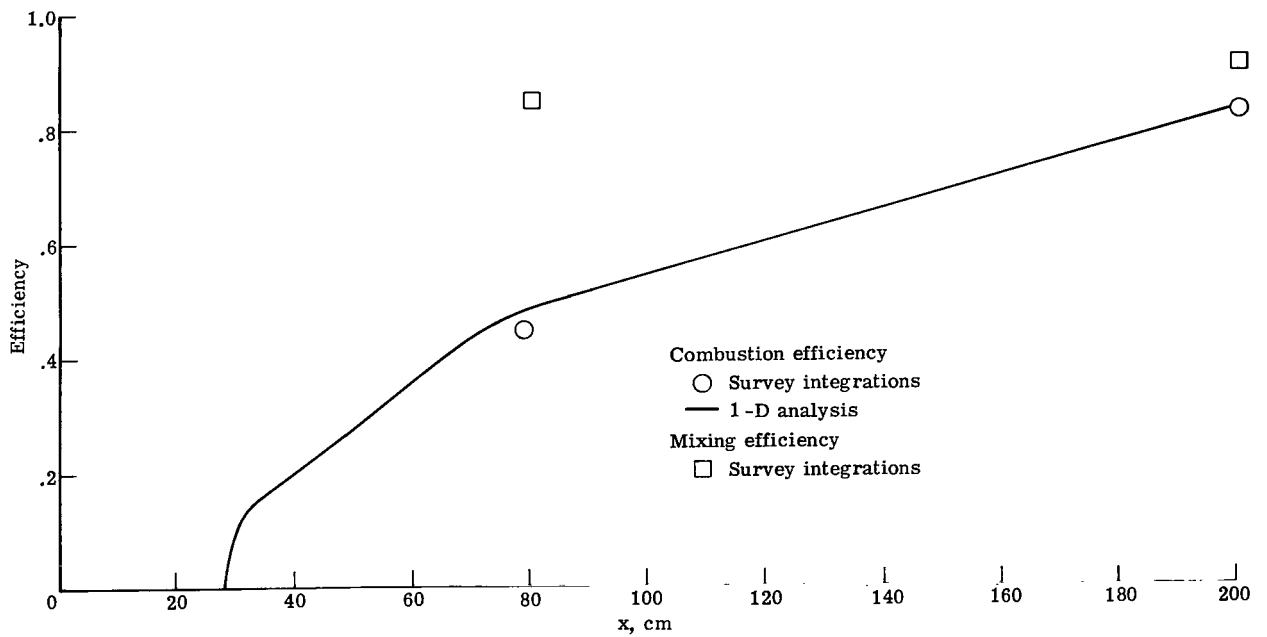Figure 17.- Lateral fuel and air distributions.   Configuration I; ϕ = 0.97.
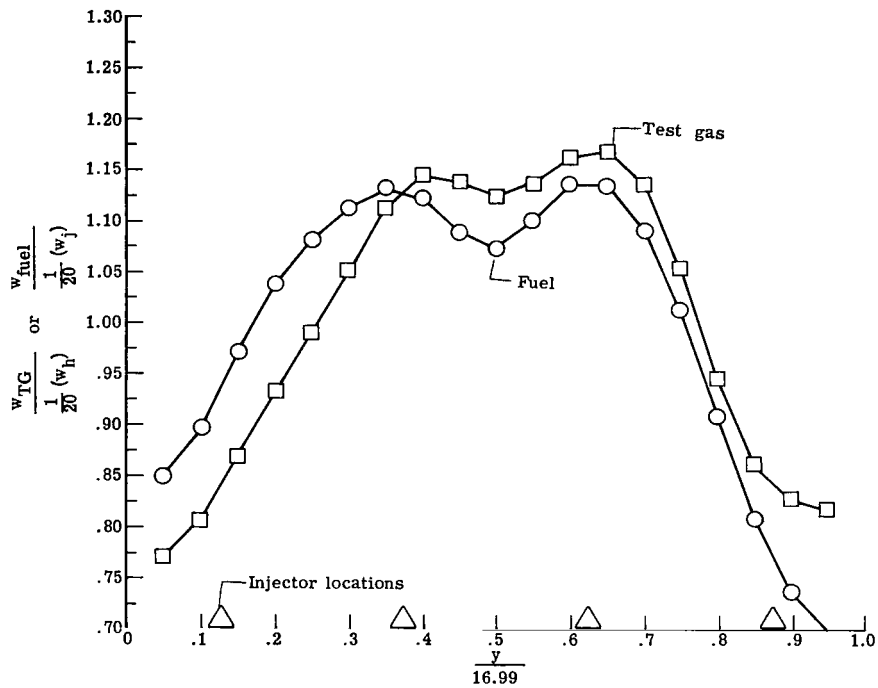
(c) Third duct exit; x = 200.7 cm.

Figure 17.- Concluded.

(a) Configuration I; injection from both walls; $\phi = 0.97$.

(b) Configuration II; $\phi_B = 0.47$.

Figure 18.- Longitudinal variation of combustion efficiency.

1. Report No. NASA TP-1174	2. Government Accession No.	3. Recipient's Catalog No.
4. Title and Subtitle INTERACTION BETWEEN STEP FUEL INJECTORS ON OPPOSITE WALLS IN A SUPERSONIC COMBUSTOR MODEL		5. Report Date May 1978
		6. Performing Organization Code
7. Author(s) Charles R. McClinton		8. Performing Organization Report No. L-11811
		10. Work Unit No. 505-05-41-08
9. Performing Organization Name and Address NASA Langley Research Center Hampton, VA 23665		11. Contract or Grant No.
12. Sponsoring Agency Name and Address National Aeronautics and Space Administration Washington, DC 20546		13. Type of Report and Period Covered Technical Paper
		14. Sponsoring Agency Code

15. Supplementary Notes

16. Abstract

   Results are presented from an experimental investigation of perpendicular, hydrogen fuel injection and combustion from opposing walls in a scramjet combustor model using a longitudinally staggered laterally inline step-injector configuration. The model represents a portion of the flow in the Langley integrated modular scramjet engine combustor operating at a flight Mach number of 7. When operating at a ratio of jet pressure to free-stream dynamic pressure of 3, the injectors produce a bulk equivalence ratio of unity. This investigation represents part of a continuing study of the modular engine fuel injectors and is specifically designed to eliminate the adverse lateral pressure gradient observed at the injector location in a previous test. Flow survey contours at three axial locations, ranging from one-third of the engine combustor length to the total engine combustor length, are used to determine mixing efficiency and fuel distribution. Wall static pressures are analyzed by using one-dimensional theory to determine the combustion efficiency. Results show a significant improvement over previous injector designs tested in this duct geometry.

17. Key Words (Suggested by Author(s)) Hypersonic propulsion Fuel injection Combustion Hydrogen Scramjet	18. Distribution Statement Unclassified – Unlimited Subject Category 07

19. Security Classif. (of this report) Unclassified	20. Security Classif. (of this page) Unclassified	21. No. of Pages 60	22. Price* $5.25

THIRD-CLASS BULK RATE

U.S.MAIL

NASA